Geophys. J. Int. (2009) **177,** 259–278 doi: 10.1111/j.1365-246X.2008.04067.x

Late Quaternary rates of uplift and shortening at Baatar Hyarhan (Mongolian Altai) with optically stimulated luminescence

Edwin Nissen,[1] Richard Walker,[1] Erdenebat Molor,[2] Morteza Fattahi[3]* and Amgalan Bayasgalan[2]

[1]*COMET, Department of Earth Sciences, University of Oxford, Parks Road, Oxford* OX1 3PR, *UK. E-mail: ed.nissen@earth.ox.ac.uk*
[2]*Mongolian University of Science and Technology, Ulaan Baatar, Mongolia*
[3]*Oxford University Centre for the Environment, South Parks Road, Oxford* OX1 3QY, *UK*

Accepted 2008 November 21. Received 2008 August 21; in original form 2008 March 14

SUMMARY

We investigate mountain building in the Altai range of western Mongolia, focusing on Baatar Hyarhan, a NW-trending massif bounded by active thrust faults. Our primary aims are to describe how thrusting has evolved over time, to calculate late Quaternary slip rates by dating offset alluvial markers with optically stimulated luminescence (OSL) and to compare these late Quaternary rates with measurements of deformation on decadal and geological timescales. Patterns of topography and drainage suggest that Baatar Hyarhan has grown in length and has propagated laterally from the SE towards the NW over time. On the NE side of the massif, the range-bounding Zereg fault appears active only along younger parts of Baatar Hyarhan; next to the oldest, SE part of the massif faulting has migrated into the adjacent Zereg Basin, where it has uplifted low, linear ridges of folded sediment, known locally as forebergs. On the SW side of the massif, only the range-bounding Tsetseg fault appears active. Using OSL, we establish ages of ∼15, ∼20 and ∼85 kyr for alluvial deposits cut by these faults. These ages are close to those of alluvial markers in the separate Gobi Altai range, suggesting that periods of fan and terrace formation may correlate over wide tracts of Mongolia, presumably under the primary control of climate. Combining our OSL ages with offsets measured with differential GPS, we calculate Late Quaternary slip rates across forebergs in the Zereg Basin and across the range-bounding Zereg and Tsetseg faults. Uncertainties in fault dip (due to lack of clear fault exposures) and burial ages (due to incomplete resetting of the luminescence clock) mean that the exact slip rates are poorly constrained. Nevertheless, the vertical displacement rates we calculate across the Zereg and Tsetseg range-front faults—0.2–0.6 and 0.1–0.4 mm yr^{-1}, respectively—are at the lower end of long-term (∼5 Myr) estimates of 0.4–0.8 and 0.3–0.7 mm yr^{-1}, respectively. Vertical rates of deformation may, therefore, have remained constant over the past ∼5 Myr, but equally the late Quaternary rates might be lower than the geological ones. This possible discrepancy could be accounted for if some of the shortening has shifted away from the range-front faults onto other nearby structures. The forebergs in the eastern Zereg Basin are an obvious candidate, but they show at least 10 km cumulative shortening (which would take a few Ma to accumulate at late Quaternary rates) and cannot simply be regarded as the latest stage of outward mountain growth. The total Late Quaternary shortening rate across all three areas of faulting is 0.7–2.4 mm yr^{-1}, making up between one tenth and one third of the ∼7 mm yr^{-1} convergence across the whole Altai range.

Key words: Geomorphology; Continental neotectonics; Fractures and faults; Kinematics of crustal and mantle deformation; Asia.

1 INTRODUCTION

The Altai mountains of western Mongolia form the northernmost region of active continental shortening within the India–Eurasia collision zone, around 2500 km north of the Himalaya (inset, Fig. 1). In contrast to the Himalaya and Tien Shan ranges to the south, which involve thrust faulting perpendicular to the convergence direction, shortening across the Altai is thought to be achieved by the anticlockwise vertical-axis rotations of N- to NW-trending right-lateral strike-slip faults (Baljinnyam *et al.* 1993; Bayasgalan *et al.* 2005). This paper comprises an early attempt to study the evolution of

*Now at: Institute of Geophysics, Tehran University, Kargar Shomali, Tehran, Iran.

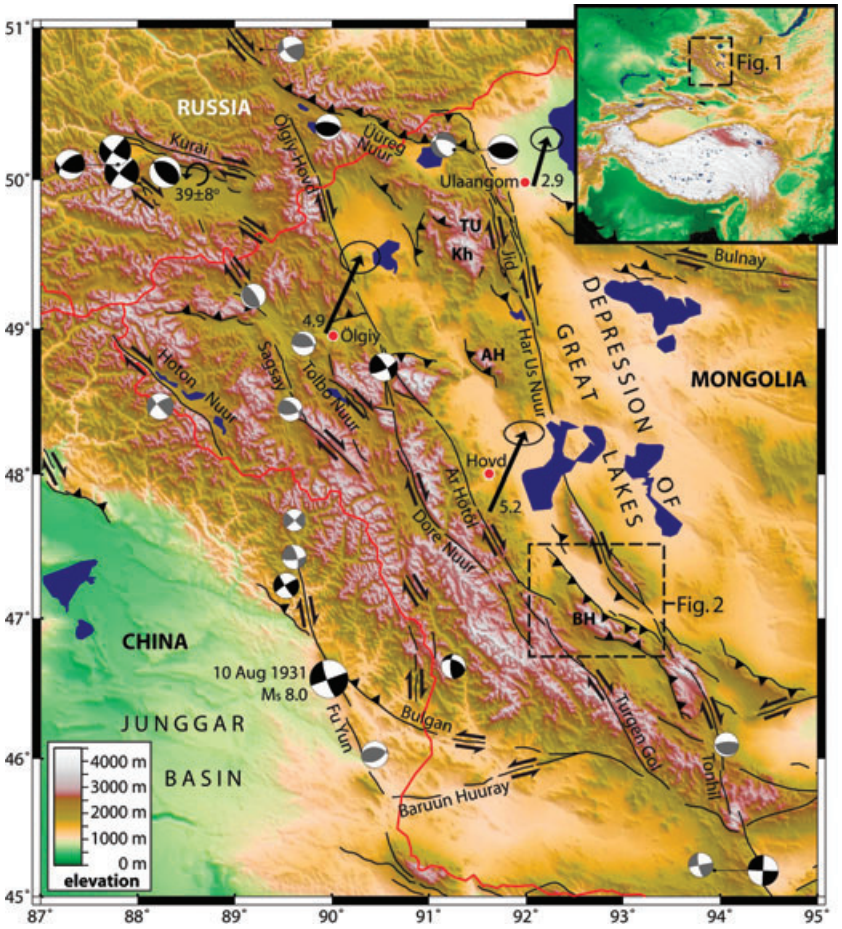

Figure 1. Earthquake ($M_w \geq 5$) focal mechanisms, GPS vectors and major active faults in the Altai mountains, plotted on shuttle radar topography mission (SRTM) topography, artificially shaded from the NE, in a Mercator projection. Black mechanisms represent earthquakes modelled with seismic waveforms or first motions (see Bayasgalan *et al.* 2005; Nissen *et al.* 2007), grey mechanisms are from the Harvard CMT catalogue (1977–2007), though for simplicity we exclude six M_w 5.0–5.2 aftershocks of the 2003 Siberian Altai sequence. All earthquakes are plotted at the latitude and longitude given in the updated version of the Engdahl *et al.* (1998) catalogue. Arrows represent GPS velocities (mm yr^{-1}) relative to stable Eurasia with 95 per cent confidence ellipses (Calais *et al.* 2003), whereas the curly arrow shows the location of palaeomagnetic measurements of anticlockwise rotations in the NW Altai (Thomas *et al.* 2002). Many high massifs are located along the large strike-slip faults, which commonly show a significant reverse component. However, a number of massifs in the eastern Altai have instead been uplifted by thrusting; these include Altun Hühay Uul (AH), Baatar Hyarhan (BH), Kharkhiraa (Kh) and Türgen Uul (TU).

faulting in the range and place constraints upon the rates of deformation. A better understanding of these kinematics may highlight processes common to other areas of distributed, rotating strike-slip faults, which include California (Schermer *et al.* 1996) and eastern Iran (Walker & Jackson 2004).

The specific focus of this study is active faulting around the margins of Baatar Hyarhan, a major massif in the southeastern Altai (Fig. 1). Baatar Hyarhan is not associated with any of the major strike-slip faults in the Altai, and its uplift is instead accommodated by a series of thrust faults exposed along its margins and in the surrounding basins. Several of these thrusts break the surface, producing clear scarps through Late Quaternary alluvial deposits. This contrasts with many other regions of continental thrusting, where shortening in the uppermost sedimentary layers is often taken up by folding, making it difficult to study the underlying 'blind' thrusts using surface measurements (e.g. Yielding *et al.* 1981).

Our first aim is to describe the contrasting styles of shortening around the margins of Baatar Hyarhan, and interpret how this faulting has evolved over time. In particular, we make use of 2.5 m-pixel Satellite Pour l'Observation de la Terre (SPOT 5) data, which provides details that are difficult to uncover with lower-resolution images or fieldwork. A second aim is to test the applicability of optically stimulated luminescence (OSL) for dating alluvial deposits cut by the faults. Most slip-rate studies in Mongolia have relied on *in situ* produced cosmogenic ^{10}Be for dating fan deposits (e.g. Ritz *et al.* 2006), but this method contains inherent assumptions (about the inherited level of ^{10}Be, its long-term production rate and the rate of erosion), and it is useful to test independent dating methods in a similar environment.

With OSL we calculate Late Quaternary displacement rates on these thrust faults at Baatar Hyarhan—the first to be published anywhere in the Altai—allowing us to put the faults into a regional context. Another advantage of Baatar Hyarhan as a study area is that its long-term cooling history has already been determined through apatite fission-track and (U-Th)/He thermochronology (Vassallo 2006). These results, summarized in Section 3.2, provide us with constraints on the initiation of uplift-related exhumation and permit the comparison between Late Quaternary and geological rates of deformation.

As well as providing ages for fault slip rate calculations, dating Late Quaternary alluvial deposits yields important information about past climate. In the Qilian Shan mountains of northeastern

Tibet, major periods of strath terrace formation occurred at the transitions from cold and dry glacial periods to warmer and wetter interglacials (Pan *et al.* 2003). A similar climatic control on alluvial fan aggradation has also been proposed for the Gobi–Altai range, where pulses of fan building can be correlated over areas many tens of kilometers wide (Vassallo *et al.* 2005; Ritz *et al.* 2006). Our OSL dating will allow us to observe whether periods of alluvial fan and river terrace formation in the eastern Altai range correlate with those in neighbouring regions of central Asia.

2 TECTONIC SETTING

The Altai range trends NW across western Mongolia and neighbouring parts of China, Russia and Kazakhstan and is one of the major mountain belts within the India–Eurasia collision zone (inset, Fig. 1). The range is surrounded by flat, low-lying and apparently undeforming regions—the vast Kazakh Platform to the north and west, the Junggar Basin to the south and a collection of smaller basins known as the Depression of Great Lakes to the east. The onset of India-related deformation in the Altai is poorly constrained; coarsening sedimentation in basins in and around the range points to initial range uplift some time during the Late Oligocene or early Miocene (Devyatkin 1974, 1981; Howard *et al.* 2003), whereas apatite fission-track modelling places it some time during the Miocene or Pliocene (De Grave & Van den haute 2002; Yuan *et al.* 2006).

There is little GPS data by which to constrain the present-day deformation of the Altai, the three arrows plotted on Fig. 1 representing the only measurements taken within the range (Calais *et al.* 2003). However, the difference between velocities (relative to Eurasia) at Urumqi, in the southern Junggar Basin ($\sim$10 mm yr^{-1}) and at Ulaangom, in the Depression of Great Lakes ($\sim$3 mm yr^{-1}), suggests the Altai currently accommodates $\sim$7 mm yr^{-1} of NNE-directed shortening (Calais *et al.* 2003). The Altai thus makes a significant contribution toward the 35–40 mm yr^{-1} total India–Eurasia convergence, also constrained by GPS (e.g. Chen *et al.* 2000; Wang *et al.* 2001; Sella *et al.* 2002).

Much of the active faulting in the Altai has been mapped using satellite imagery, revealing an anastomosing pattern of NNW striking right-lateral strike-slip faults (Tapponnier & Molnar 1979; Cunningham 2005). Earthquakes during instrumental period are consistent with this style of deformation, whereas several spectacular ruptures, preserved for up to many hundreds of years, attest to similar movements in the historical past (e.g. Baljinnyam *et al.* 1993; Walker *et al.* 2006). The discrepancy between earthquake slip vectors and the overall convergence direction suggests that regional shortening is achieved by anticlockwise, vertical-axes rotations of the right-lateral strike-slip faults and the slivers of crust between them (Baljinnyam *et al.* 1993; Bayasgalan *et al.* 2005). The limited palaeomagnetic data currently available, from a single study in the Siberian Altai (Thomas *et al.* 2002, Fig. 1), support this kinematic model. This style of shortening may be governed by the $\sim$NW-trending structural fabric of the range, which is thought to be inherited from the Palaeozoic accretion of continental fragments and arc terranes (Sengör *et al.* 1993; Cunningham 1998).

Many of the strike-slip faults show a significant reverse component and thus contribute to long-term uplift within the range. This reverse component may be a direct result of the vertical-axis crustal rotations, or it may be introduced by local deviations in the geometry of the structural fabric. In addition, many of the high mountains at the northern and southern ends of the range relate to thrust terminations of the strike-slip faults (Bayasgalan *et al.* 1999a; Walker *et al.* 2006). Peaks are characterized by flat summit plateaus, up to $\sim$4–4.5 km in elevation. These are also observed in northern, central and southern Mongolia (as well as neighbouring parts of Russia and China) and are thought to be remnants of a vast erosional surface. According to apatite fission-track studies, this peneplain formed during the Jurassic or Cretaceous period (De Grave & Van den haute 2002; Yuan *et al.* 2006; Vassallo *et al.* 2007a) and has since undergone more than 100 Myr of tectonic quiescence before the onset of Late Cenozoic deformation (Jolivet *et al.* 2007). For our purposes, the peneplain surface acts as a convenient marker of the cumulative vertical deformation within the region.

Several of the highest massifs in the Altai are not situated along strike-slip faults; in particular, there are a number of isolated ranges in the eastern Altai that show clear thrust scarps through Quaternary deposits along their margins (some of these are labelled in Fig. 1). Baatar Hyarhan is the southernmost of these massifs.

3 OVERVIEW OF BAATAR HYARHAN AND SURROUNDING BASINS

Baatar Hyarhan (also referred to as Baataryn Nuruu or Baatar Khairkhanii) trends NW–SE, is around 100 km in length and up to 20 km wide and reaches a maximum elevation of 3984 m, more than 2 km higher than the Zereg Basin ($\sim$1100 m) to the northeast and the Tsetseg Basin ($\sim$1700 m) to the south (Figs 2 and 3a). In this section, we provide an overview of the bedrock geology, uplift history and geomorphology of the range.

3.1 Bedrock geology

The bedrock of Baatar Hyarhan comprises Cambrian granite in the core of the range, surrounded by Palaeozoic volcanics, metamorphics and sediments (Zaitsev *et al.* 1989). Because these rocks trend NW–SE, there is little variation in bedrock lithology along the length of the range. The surface geology of the surrounding depressions primarily consists of Quaternary alluvium shed from Baatar Hyarhan and other nearby massifs. In addition, parts of the Zereg Basin contain low, NW-trending ridges, known locally as 'forebergs', that expose older Mesozoic and Tertiary sediments (Howard *et al.* 2003). Forebergs exist in a number of other places in Mongolia, especially along the Gobi–Altai range (in the southern part of the country), where they were first described (Florensov & Solonenko 1963). Resulting from thrusting and folding of the Earth's surface in areas of thick alluvial cover, they form adjacent (and parallel) to range-bounding thrust or oblique-slip faults and are thought to represent the propagation of these faults into their forelands (e.g. Owen *et al.* 1997, 1999; Bayasgalan *et al.* 1999b). There are two sets of forebergs in our study area: one near the Bumbat Nuruu range, on the eastern side of the Zereg Basin (Fig. 3b), and one close to Baatar Hyarhan itself, on the southern side of the depression (Fig. 3c).

3.2 History of uplift

The cooling history of Baatar Hyarhan has been quantified through apatite fission-track (AFT) and (U-Th)/He measurements of bedrock samples from the Boorguinn Gol valley in the central section of the range (Vassallo 2006, Fig. 8). AFT central ages range from 154 to 192 Myr, whereas those from analysis of (U-Th)/He range from 77 to 127 Myr. Temperature–time paths obtained by

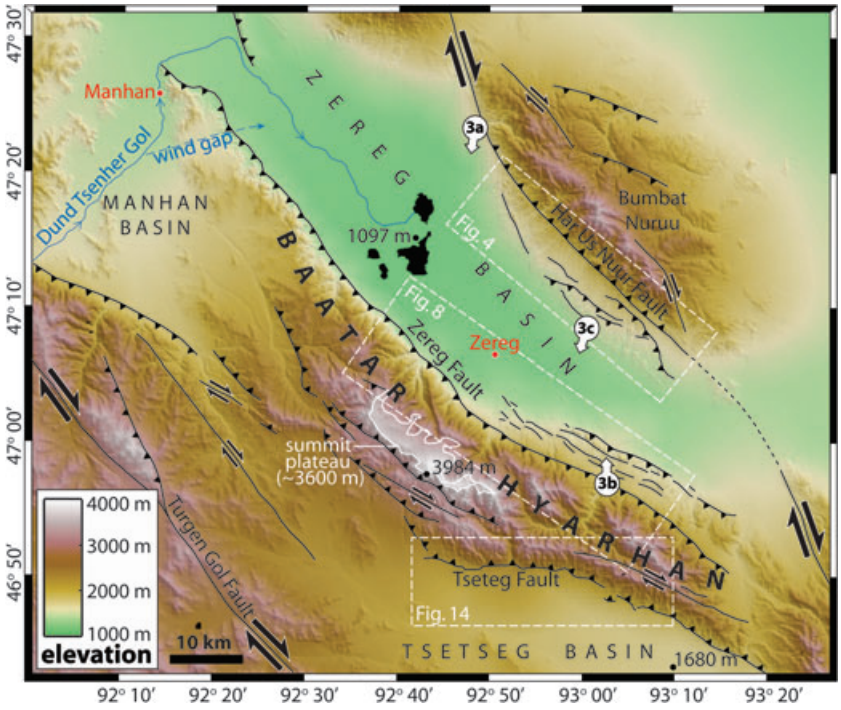

Figure 2. SRTM topography and faults of the Baatar Hyarhan range and surrounding basins, displayed in the local UTM zone (46) projection (as are subsequent maps) and artificially sun-shaded from the NE. The location of the map is shown as a black rectangle on Fig. 1. The dashed blue line shows a former course of the Dund Tsenher Gol river, through what is now an air gap in the northwestern part of the range.

modelling this data confirm the Late Mesozoic age of the summit plateau and place the latest, Late Cenozoic stage of uplift at ∼5–1 Ma.

This is somewhat younger than an estimate of the onset of Late Cenozoic uplift based on sedimentological grounds (Howard *et al.* 2003). Strata exposed in the S Zereg Basin forebergs show coarsening grain sizes, together with a switch to a southwesterly source during the Miocene (23–5 Ma). This may represent the earliest growth of Baatar Hyarhan, although there are uncertainties in the exact age of the material, as well as its origin (which might lie in ranges other than Baatar Hyarhan, such the mountains SW of the Tsetseg Basin).

3.3 Range geomorphology: lateral propagation?

The topographic characteristics of Baatar Hyarhan change notably along its length (Fig. 2). The SE section (east of 92°50′E) is the most heavily eroded part of the massif, containing sharp peaks and ridges of up to ∼3500 m elevation, separated by deep, wide valleys. In contrast, the central section of the range (between 92°35′E and 92°50′E) contains a wide summit plateau at ∼3600 m elevation (Fig. 3a), part of the vast Late Mesozoic peneplain surface observed throughout western and central Mongolia (Jolivet *et al.* 2007). In the final section of the massif (west of 92°35′E), the elevated topography—including remnants of the peneplain—gradually tails off towards the NW, dying out completely near the town of Manhan. Given that neither lithology nor climate varies significantly along the length of Baatar Hyarhan, the deep incision observed in the SE part of the range suggests that this area has been subjected to erosion for longer than the central and NW sections, where the peneplain is preserved.

Near Manhan, the Dund Tsenher Gol river flows round the northwestern tip of the range on its way into the Zereg Basin (Fig. 2). Around 12 km to the south, a pronounced, linear depression (or wind-gap) indicates a probable former course of the river through what is now an uplifted part of the range. There are a number of possible reasons for the northwestward shift in the course of the Dund Tsenher Gol river over time. It might either reflect the lateral growth of the Baatar Hyarhan from the SE toward the NW over time (Keller *et al.* 1998, 1999), or a lower uplift rate at the northwestern end of the massif or alternatively some past climatic change that reduced the river incision rate. Taken together with the lateral variation in the dissection of the summit peneplain, however, we support the view that the range has propagated from the SE towards the NW over time.

4 ACTIVE FAULTING

We now investigate variations in the style of shortening along the margins of Baatar Hyarhan, focusing on four contrasting sections of faulting. If the range has grown northwestwards over time (Section 3.3), then these changes help constrain how faulting in the region evolves over time. For three out of four sections, we are also able to establish rates of uplift and horizontal shortening, using alluvial fans and river terraces as markers of fault slip and OSL to date these surfaces.

In Section 4.1, we study shortening across the forebergs in the eastern Zereg Basin; these trend parallel with the highest part of the massif but lie about 20 km away to the NE. In Section 4.2, we focus on the forebergs in the southern Zereg Basin, which lie next to the most eroded (SE) part of Baatar Hyarhan (in this case, no dateable material is found; so, we do not provide constraints on rates of deformation). In Section 4.3, we investigate thrusting along the range-bounding Zereg fault, focusing on thrust scarps adjacent to the highest part of the range. Finally, we switch attention to the SW side of the range, studying the range-bounding Tsetseg fault in Section 4.4.

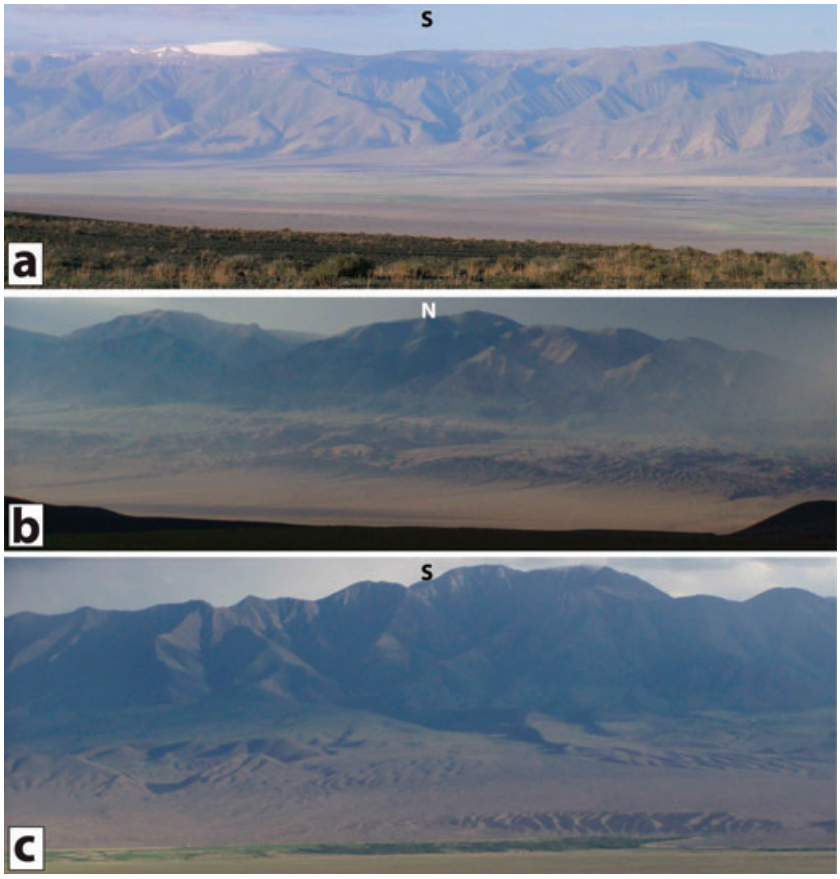

Figure 3. Field photographs of Baatar Hyarhan and nearby forebergs, taken from the locations plotted on Fig. 2. (a) View S from 47°23′45″N 92°49′12″E, looking across the Zereg Basin (elevation ∼1100 m) toward the central Baatar Hyarhan massif with its flat summit peneplain and small glacier (at ∼3600 m). (b) View N from 46°57′06″N 93°02′53″E toward part of the E Zereg Basin forebergs, with the Bumbat Nuruu mountains behind. (c) View S from 47°08′06″N 93°00′42″E toward the western part of the S Zereg Basin forebergs, with SE Baatar Hyarhan behind. Note the sharper peaks and ridges of this part of the Baatar Hyarhan massif in comparison with the central part, shown in (a).

It should be noted that in all four study areas, we primarily consider the reverse component of motion. There are no obvious indications in the geomorphology of a right-lateral strike-slip component to any of the main active thrusts, although given the tectonic setting, we do not rule out there being one, in particular, on the SW side of the range (discussed in Section 4.4).

4.1 Eastern Zereg Basin forebergs

The eastern Zereg Basin contains a series of foreberg hills in which Mesozoic and Tertiary sediments have been uplifted next to the SW margin of the Bumbat Nuruu mountains (Figs 3b and 4). At first glance, these hills resemble forebergs of Bumbat Nuruu, but a closer inspection reveals a series of fault and fold scarps that all face northeastward; furthermore, the main folds also verge towards the northeast. This provides strong evidence that the underlying thrusts dip southwest, towards Baatar Hyarhan (e.g. Howard *et al.* 2003).

4.1.1 Stratigraphy

Several perennial streams sourced from Bumbat Nuruu are actively incising into the forebergs, creating a badlands style terrain in which the stratigraphy of the Mesozoic and Tertiary sediments is well exposed (Figs 5 and 6a). This stratigraphy is described in detail by Howard *et al.* (2003), although there may be considerable uncertainties in the precise ages of the sediments, which were estimated using, sometimes, sparse fossil remains. The oldest strata are Lower Cretaceous and consist of fine-grained lacustrine and floodplain deposits (divided into Yellow Sandstone and Red Bed units) sourced both from the NW and SE. This drainage was oriented axially to structures observed in and around the basin today, leading Howard *et al.* (2003) to suggest that the same faults were active in the Mesozoic, though with a normal sense of motion. For a short distance (150 m) of their mapped section, the authors trace a 20° angular unconformity between the Lower Cretaceous Red Bed unit and overlying Oligocene sandstones, which are the oldest Tertiary sediments exposed in the area. They suggest that this may represent the same erosion surface that is preserved as the flat summit plateaus of Baatar Hyarhan and other Altai massifs.

The Tertiary sediments coarsen upwards from the Oligocene sandstones into Miocene, Pliocene and Pleistocene conglomerates. Palaeocurrent data show a switch from sources to the NW and SE (axial to local faults) to a source to the NE in the Miocene. Together with the coarsening in sedimentation, this suggests that Bumbat Nuruu (lying NE of the forebergs) began uplifting at this time. Quaternary fluvial and alluvial conglomerates were deposited unconformably over the Cretaceous and Tertiary strata and are preserved today as abandoned river terraces and alluvial fans. There are three prominent levels of strath terrace in the central section of

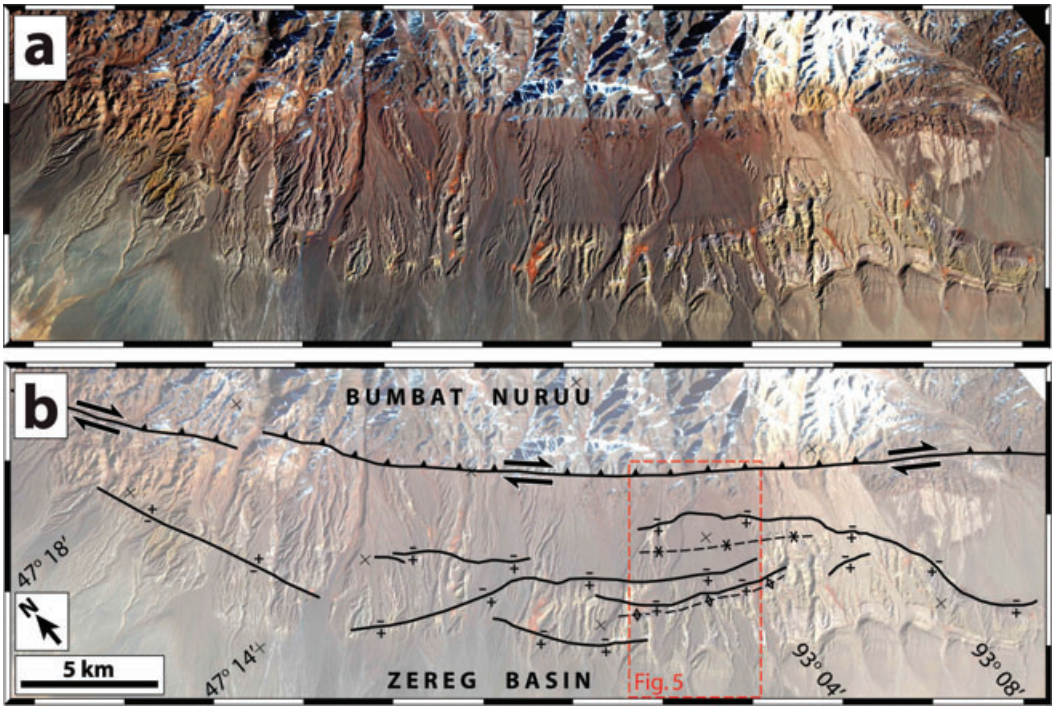

Figure 4. (a) ASTER image (15 m resolution; RGB 321) of the eastern Zereg Basin forebergs. The location of the map is shown as a dashed box on Fig. 2. (b) The same view, with scarps plotted as thick solid lines (± indicates the sense of displacement) and fold axes as thin dashed lines.

the forebergs, the area which we now focus on. We call these terraces EZ1, EZ2 and EZ3, in increasing order of age and elevation (Fig. 5b).

4.1.2 Structure

Next we describe the geological structure across this same section of forebergs, using data from Howard *et al.* (2003) supplemented by our own measurements (taken from a narrow canyon plotted on Fig. 5b). The Cretaceous and Tertiary sediments are folded into a NE-verging anticline and syncline pair (Fig. 7a). Crossing the anticline, we observe abrupt changes in the dip of these strata, starting with 0° in Quaternary alluvium at the SW edge of the forebergs and stepping progressively upwards to ∼20°SW (in the Pleistocene–Miocene conglomerates), ∼40°SW (in the Oligocene sandstones and the Cretaceous Red Bed unit) and ∼60°–80°SW (in the Cretaceous Yellow Sandstone unit), as we approach the core of the fold (Fig. 6b). The NE limb of the anticline is initially overturned, before strata shallow out NE-wards into the syncline. The steep-sided canyons that expose the bedrock so well in the SW part of the geological cross-section do not extend as far NE as the syncline; so, we extrapolate measurements taken by Howard *et al.* (2003) ∼2 km along strike to the SE (near 47°09′N 93°05′E). It is not clear whether the syncline contains abrupt changes in dip, similar to those observed in the anticline.

Three parallel, NE-facing scarps cross the Quaternary river terraces in our study area, each delineating a sharp change in the amount of river incision (Fig. 5). We refer to these as scarps A (in the southwest), B (in the centre) and C (in the northeast).

Scarp A is situated within a section of steep, 60°–80° SW-dipping Cretaceous Yellow Sandstone strata close to the core of the anticline. Although we find no direct exposures of the scarp in cross-section, the strong NE-ward fold vergence suggests that it represents the surface expression of an active, SW-dipping thrust fault (Howard *et al.* 2003). We call this thrust 'fault A'. Along-strike to the NW and SE, it becomes blind, but the tightly folded core of the anticline remains the same Yellow Sandstone unit. We assume, following the work of Howard *et al.* (2003), that the thrust propagated towards the surface from a detachment at the base of this unit. In this model, the anticline formed as a fault-propagation fold above the tip of this thrust, which has since broken through to the surface (Suppe & Medwedeff 1990). We also consider the abrupt changes in the dip of sedimentary strata to reflect abrupt changes in the dip of the underlying thrust, consistent with the fault-bend folding model of Suppe (1983). This would suggest that the fault A soles into a flat detachment under the Zereg Basin at depths of around 1.5–2 km (Fig. 7a).

Scarp B is situated about 1 km northeast of scarp A, probably within NE-dipping strata within the SW limb of the syncline. There is little bedrock exposure in this area, and the scarp is not described by Howard *et al.* (2003). However, the same scarp can be followed on satellite imagery for a distance of ∼10 km northwest of our study area and does not appear to outcrop within the same sedimentary unit along its whole length. This suggests that it represents another SW-dipping thrust ('fault B')—perhaps a shallow splay off fault A—rather than localized bedding-plane slip.

Scarp C is situated a further ∼2 km northeast of scarp B (in another area of poor bedrock exposure) and can be followed over a total distance of ∼15 km, finally ending in the far southeastern section of forebergs. Although not exposed in cross-section within our study area, Howard *et al.* (2003) interpret it as a SW-dipping thrust ('fault C'), based on their observations 2 km along strike to the NE, where it comes to the surface amongst Yellow Sandstones dipping ∼45°–65° SW. The repetition of the Yellow Sandstone is most easily explained if fault C propogated to the surface along the base of this unit, perhaps from the same detachment under the Zereg Basin as fault A (Fig.7a).

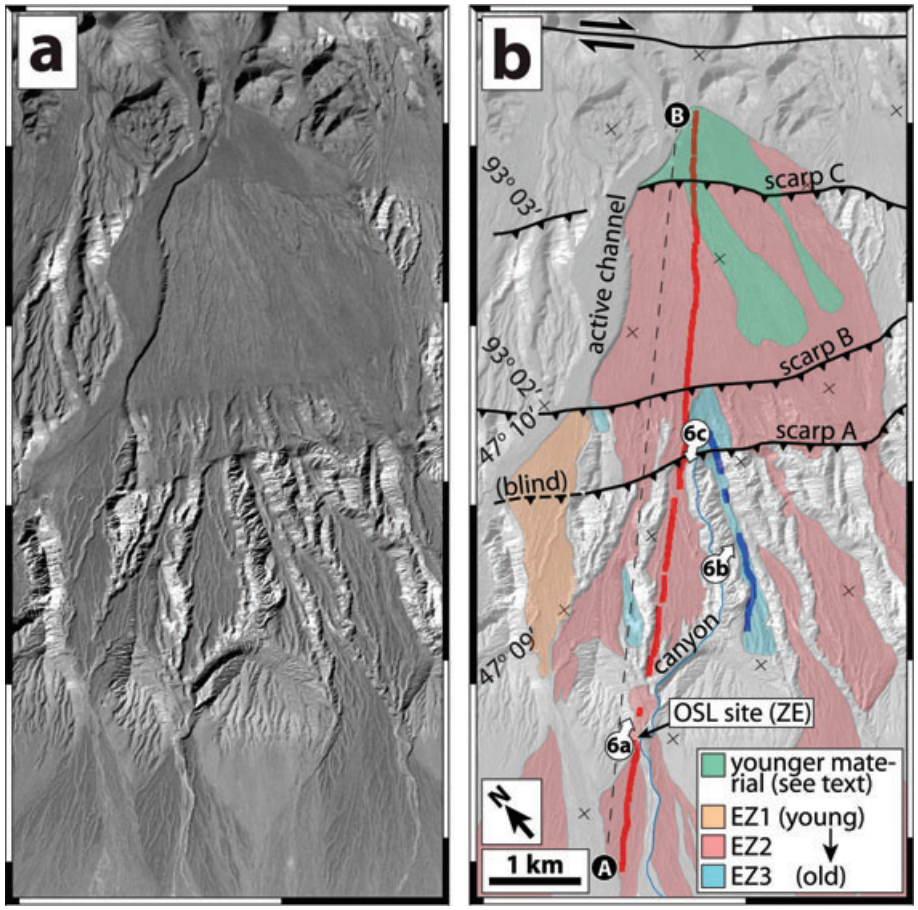

Figure 5. (a) SPOT 5 image (2.5 m resolution) of the central section of forebergs in the eastern Zereg Basin. The location of the map is shown as a dashed box on Fig. 4. (b) The same view, with Late Quaternary terrace levels and fault scarps superimposed. Cretaceous and Tertiary sediments are well exposed in the systems of canyons that lie between the preserved terrace remnants. The geology exposed in the canyon marked with a thin blue line is projected onto the line A–B and plotted in Fig. 7(a). The small red and blue squares are points measured in differential GPS profiles of the EZ2 and EZ3 surfaces, respectively; elevations, again projected onto A–B, are plotted in Fig. 7(b).

4.1.3 Terrace profiles

Using differential GPS we produced topographic profiles of the preserved remnants of the EZ2 and EZ3 terraces. The position and elevation of a roving GPS receiver were measured relative to a second, stationary receiver. These relative heights are accurate to a few centimetres. Profile points are plotted on Fig. 5(b), and the profiles themselves are shown in Fig. 7(b), with EZ2 data in red and EZ3 in blue. The slope of the EZ2 terrace steepens from ∼3.4° at the SW end of the profile to ∼6.9° at the NE end. Fitting a quadratic line to data farthest from the faults (at the far SW and NE ends of the profile) provides an estimate of the original shape of the surface before deformation. Subtracting this presumed undeformed profile from the observed EZ2 and EZ3 surfaces gives a sense of the shape and magnitude of deformation that the terraces have undergone since abandonment (Fig. 7c). There are changes in the slope of both these profiles close to the places where the underlying strata suddenly steepen (from 0° to 20° and from 20° to 40° SW), supporting the notion that the abrupt changes in the dip of the exposed sediments reflect changes in the dip of the underlying thrust.

In addition, the EZ2 surface shows clear vertical displacements across scarps A and B (Fig. 7d). The former consists of a sharp, ∼20.5 m vertical offset (up to the SW). The latter consists of a further offset of ∼17.5 m, though of this only ∼7.5 m is preserved as a sharp offset at the scarp itself. The surface appears pristine; so, this difference is unlikely to reflect erosion of the scarp; instead, the remaining 10 m vertical displacement might be achieved by folding of the hangingwall sediments.

In the highest part of the topographic profile, there appears no abrupt displacement in EZ2 across the trace of scarp C (Fig. 7c). However, close inspection of SPOT imagery (made available to us only after we visited the study area) reveals that sections of this scarp, including the part we profiled, have been incised by more recent drainage systems and replaced with younger material (visible as darker areas in Fig. 5a and shaded in green in Fig. 5b). These younger deposits do not preserve the full deformation of the EZ2 surface; so, to estimate the displacement of EZ2, we instead extrapolate slopes from a few hundred metres up- and downsection from the eroded scarp. This yields a ∼12.5 m vertical offset of the EZ2 surface across the fault, up to the SW (Fig. 7e).

4.1.4 Late Quaternary displacement rates

Following the procedures outlined in the Appendix (Section A1) we sampled the EZ2 terrace for OSL dating. Our sample (labelled ZE) comes from a 10-cm-thick sand body exposed ∼3 m below the surface of the terrace in the side of a gully, at 47°08′09.7″N 93°00′48.5″E (Fig. 5b). This is part of a much thicker sequence of

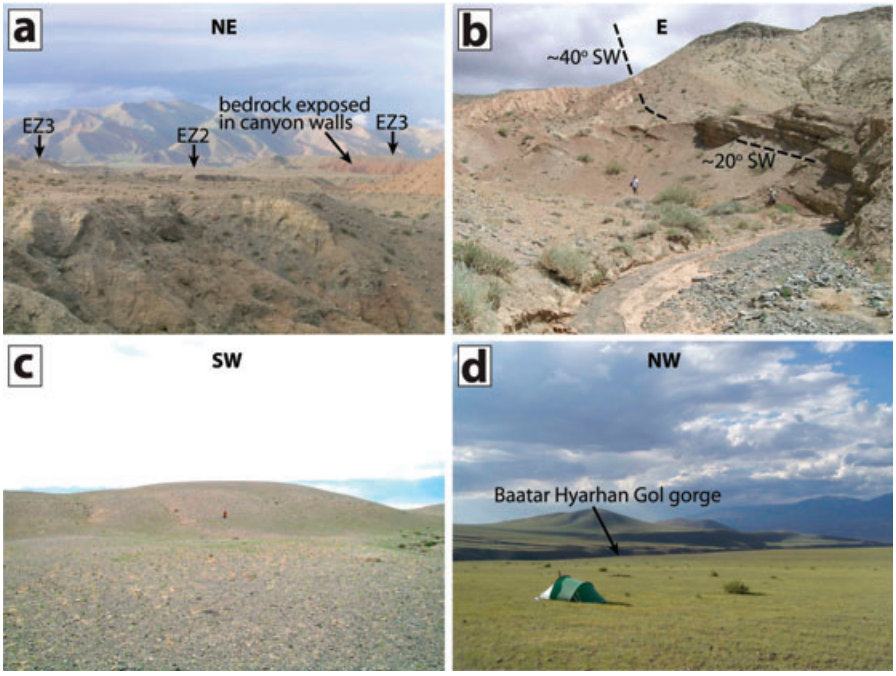

Figure 6. Photographs of forebergs in the Zereg Basin. (a) View NE from 47°08′06″N 93°00′42″E (see Fig. 5b) of badlands-style terrain in the E Zereg Basin forebergs, with the Bumbat Nuruu mountains in the distance. (b) View E from 47°08′37.1″N 93°02′14.7″E (see Fig. 5b), with two people for scale. Beds exposed in the canyon walls steepen sharply from ∼20° SW to ∼40° SW between the right and left-hand sides of the photograph. (c) View SW from 47°09′16.1″N 93°02′46.4″E (see Fig. 5b) of fault scarp A crossing the EZ2 terrace, with a person for scale. Note the relatively dense vegetation along the foot of the scarp. (d) View NW from 46°57′06″N 93°02′53″E (see Fig. 9b) of forebergs on the southern side of the Zereg depression. The foreground is the abandoned BG4 river terrace, whereas several other levels are picked out in the evening light on the far side of the Baatar Hyarhan Gol river. The mountains in the far distance (on the right-hand side of the photo) are the Bumbat Nuruu range.

sands and fine gravels (locally extensive over many tens of metres), buried beneath a single debris-flow deposit which forms the uppermost part of the terrace. Luminescence measurements were taken following the laboratory procedures described in Section A2. Individual aliquots show a well-defined peak in their measured equivalent doses (Fig. A1a). However, there is some spread to the data either side of this peak, which could signify incomplete bleaching of the sample prior to burial. Because of this uncertainty, we use the weighted mean equivalent dose to calculate the burial age; this yields an age of 84.1 $\pm$ $_{1\sigma}$ 9.4 kyr (Table A2).

Combining this age with the 20.5 m vertical scarp offset gives a vertical displacement rate of $0.24^{+0.03}_{-0.02}$ mm yr^{-1} across fault A. The fault dip lies between 60° and 80°SW, giving a horizontal shortening rate of $0.09^{+0.07}_{-0.05}$ mm yr^{-1} and a fault slip-rate of $0.26^{+0.06}_{-0.04}$ mm yr^{-1}. The 17.5 m vertical offset across fault B yields a vertical displacement rate of $0.21^{+0.02}_{-0.02}$ mm yr^{-1}. Using conservative bounds of 20°–60°SW on the fault dip, the horizontal shortening rate is $0.25^{+0.39}_{-0.14}$ mm yr^{-1}, and the slip rate is $0.32^{+0.36}_{-0.10}$ mm yr^{-1}. Finally, a vertical scarp offset of 12.5 m and a dip of 45°–65°SW gives a vertical displacement rate of $0.15^{+0.02}_{-0.02}$ mm yr^{-1}, a horizontal shortening rate of $0.10^{+0.07}_{-0.04}$ mm yr^{-1} and a slip rate of $0.18^{+0.06}_{-0.04}$ mm yr^{-1} across fault C. These displacement rates are summarized in Table 1.

In our model, faults A, B and C sole into a detachment at the base of the Yellow Sandstone unit under the Zereg Basin. In this case, the total Late Quaternary rate of slip on this detachment (and thus the total Late Quaternary shortening across the E Zereg Basin) is the sum of the slip rates on each fault, which is $0.76^{+0.48}_{-0.17}$ mm yr^{-1}. This is a minimum estimate because a proportion of the slip on the detachment may not reach the surface on the thrusts, but could be accommodated instead by folding of the uppermost sediments.

4.1.5 Onset of faulting

We now consider the onset of deformation in the eastern Zereg Basin, using our geological cross-section in Fig. 7(a) to estimate the cumulative shortening on the three faults and our Late Quaternary slip rates to extrapolate back in time. Restoring the base of the Cretaceous Yellow Sandstone unit (Fig. 7a), there is around ∼3.5 km shortening on fault A and ∼6.5 km on fault C; these are minimum estimates, as they do not account for material removed at the surface by erosion. The structure of the middle part of the cross-section is too poorly understood to constrain the total shortening on fault B.

At the calculated Late Quaternary rate of $0.76^{+0.48}_{-0.17}$ mm yr^{-1}, and discounting folding, a minimum total shortening of ∼10 km would be achieved in 8–17 Myr. Because of uncertainties in our structural model at depth, as well as the assumption that Late Quaternary slip rates are representative over the longer-term, these should be considered only approximate ages. However, they do suggest that faulting in the eastern Zereg Basin is at least a few million years in age.

4.2 Southern Zereg Basin forebergs

There is a second line of forebergs on the southern side of the Zereg Basin, adjacent to the southeastern section of Baatar Hyarhan (Figs 3c and 8). Rivers and streams incising into these hills reveal deformed Mesozoic and Tertiary sediments, although there are fewer canyons and ravines than on the eastern side of the depression and the bedrock exposure is limited in comparison. The stratigraphy, which is described by Howard *et al.* (2003), consists of Lower Cretaceous red beds (fine-grained floodplain deposits sourced from the

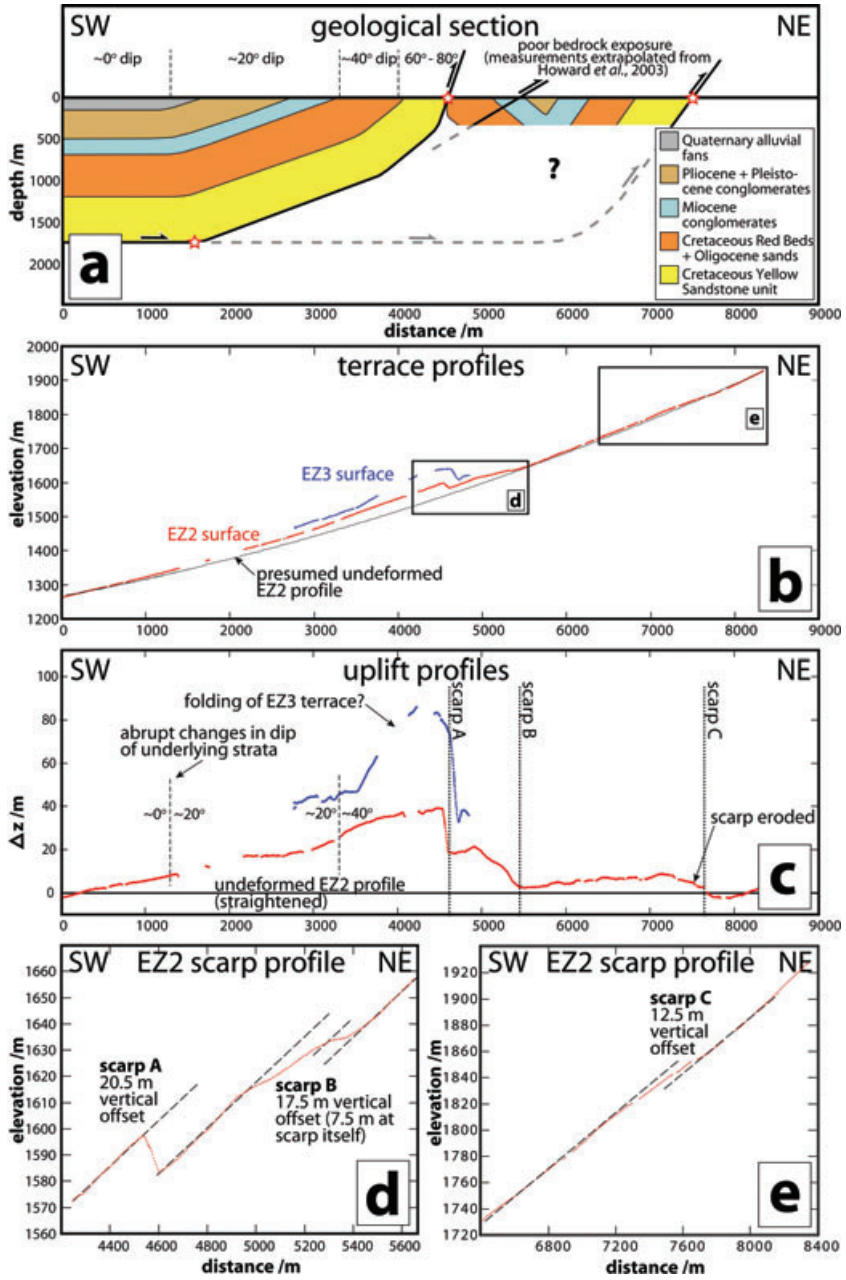

Figure 7. (a) Geological cross-section of the E Zereg Basin forebergs. Like Howard *et al.* (2003), we map the lower Cretaceous Red Bed unit and Oligocene sandstones together. Dip measurements are taken from a canyon (plotted as a thin blue line on Fig. 5b), except for the NE part where we extrapolate published data from Howard *et al.* (2003), taken near 47°09′N 93°05′E . All data are then projected onto the line A–B (plotted on Fig. 5b). The red stars show the 3.5 and 6.5 km distances required to restore the base of the Yellow Sandstone unit along faults A and C, respectively. (b) Topographic profiles of EZ2 (red) and EZ3 (blue) fan surfaces, measured with differential GPS and also projected onto the line A–B (see Fig. 5b). (c) EZ2 uplift profile, calculated by subtracting the presumed undeformed profile from the observed heights. (d) and (e) Details of the topographic profiles across the scarps A, B and C.

SE) and Miocene, Pliocene and Pleistocene alluvial fan conglomerates (sourced from the SW). As discussed in Section 3.2, the switch in palaeocurrent direction and the coarsening in sedimentation may reflect the initial uplift of Baatar Hyarhan, or perhaps other mountains SW of the Tsetseg Basin. Quaternary fluvial and alluvial conglomerates deposited unconformably over the Cretaceous and Tertiary strata are preserved today as abandoned river terraces and alluvial fans.

The forebergs are bounded on the SW side by the Zereg fault, which in this section appears degraded and may no longer be active (Fig. 8). On the NE side of the forebergs, an abrupt change in the amount of river incision marks the trace of an active, SW-dipping thrust, although west of the Baatar Hyarhan Gol river this fault is probably blind. Within the forebergs themselves, the Cretaceous and Tertiary sediments are folded into a large anticline; like Howard *et al.* (2003), we interpret this as a fault propagation fold, related to growth of the underlying thrust. In the central part of the forebergs (around the Baatar Hyarhan Gol river), dip measurements from Howard *et al.* (2003) and our own fieldwork show that this anticline verges northeastwards (Fig. 10a), although this sense of asymmetry appears to be reversed along strike to the NW. Numerous NE- and SW-facing scarps within the forebergs (Fig. 8) may

Table 1. A summary of the rates of vertical and horizontal displacement and fault slip for the five thrusts studied in Section 4. Faults A, B and C are those studied in the eastern Zereg Basin (Section 4.1). 'Offset' is the vertical displacement of alluvial fans across the fault, and 'age' is the luminescence age of these surfaces (with 1σ errors). The total shortening rate across the eastern Zereg Basin forebergs is equal to the sum of the slip rates on fault A, B and C, as described in Section 4.1.4

Fault name	Fault dip	Offset (m)	Age (kyr)	Displ. rates (mm yr^{-1})		
				Vertical	Horizontal	Fault slip
Fault A	60°–80°	20.5	84.1 ± 9.4	$0.24^{+0.03}_{-0.02}$	$0.09^{+0.07}_{-0.05}$	$0.26^{+0.06}_{-0.04}$
Fault B	20°–60°	17.5	84.1 ± 9.4	$0.21^{+0.02}_{-0.02}$	$0.25^{+0.39}_{-0.14}$	$0.32^{+0.36}_{-0.10}$
Fault C	45°–65°	12.5	84.1 ± 9.4	$0.15^{+0.02}_{-0.02}$	$0.10^{+0.07}_{-0.04}$	$0.18^{+0.06}_{-0.04}$
Zereg Fault	50°–70°	4.2–5.8	14.3 ± 5.3	$0.35^{+0.29}_{-0.14}$	$0.20^{+0.34}_{-0.12}$	$0.40^{+0.44}_{-0.17}$
Tsetseg Fault	32°–46°	2.5–3.3	20.0 ± 11.2	$0.15^{+0.23}_{-0.07}$	$0.18^{+0.42}_{-0.10}$	$0.23^{+0.48}_{-0.12}$

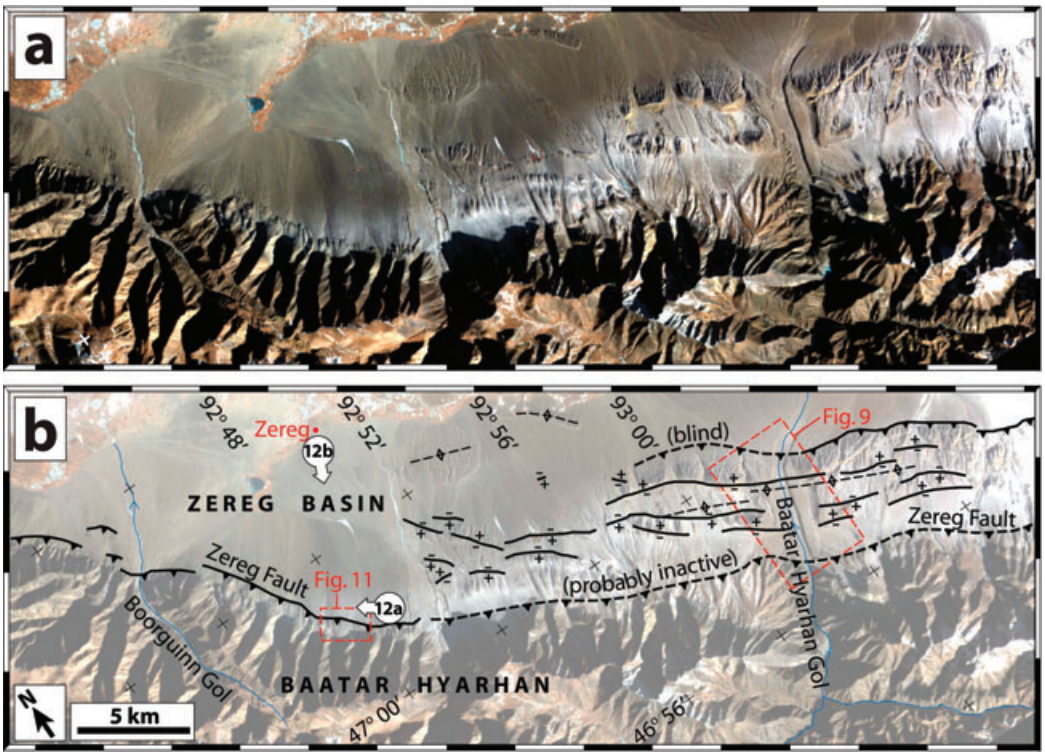

Figure 8. (a) ASTER image (RGB 321) showing faulting along the northeastern margin of Baatar Hyarhan. The location of the map is shown as a dashed box on Fig. 2. (b) The same view, with scarps plotted as thick solid lines (± indicates the sense of displacement) and fold axes as thin dashed lines. The eastern part of the Zereg fault, shown as a thick dashed line, looks degraded and may no longer be active.

represent bedding-plane slip and minor normal faulting associated with the growth of this anticline, although small thrusts and back-thrusts might also be present.

The Baatar Hyarhan Gol river, which drains much of the SE part of the range, cuts a prominent gorge through the forebergs (Figs 6d and 9). Above it, a prominent flight of abandoned river terraces are preserved (these are labelled BG1–BG8 on Fig. 9b). Using differential GPS, we produced topographic profiles of the BG7 and BG4 terraces, as well as a prominent flood level preserved about a metre above the active stream bed (Fig. 10b). These three surfaces all show clear SW-facing scarps—with vertical displacements of around 20, 4.5 and 3.0 m, respectively—at a distance of ∼3900 m along the profiles (and from the Zereg fault). This location coincides with the boundary between the Cretaceous red beds and Miocene conglomerates, and the scarp probably represents bedding-plane slip on this contact.

The BG4 terrace shows further evidence of folding (as would BG7, presumably, if it were more complete). We do not know the gradient at which BG4 was originally deposited; it may have been similar to that of the current Baatar Hyarhan Gol river bed, or perhaps steeper, if headward erosion into the peneplain has progressively lowered river gradients over time (Vassallo *et al.* 2007b). However, subtracting the slope of the current Baatar Hyarhan Gol river bed from the BG4 topographic profile provides at least an approximate indication of the shape of deformation the terrace has undergone since abandonment (Fig. 10c). Aside from the far SW end, where the BG4 surface is steep (and may actually be covered by small fan deposits derived from the slopes of Baatar Hyarhan), the maximum uplift is at a distance of 1000–2000 m along the profile. This location is offset by 1–2 km from the mapped core of the anticline, although the geological cross-section is based on sparse bedrock exposure and so, there are significant uncertainties in its exact shape.

We did not find any exposures where fine-grained sediments might be sampled for OSL dating of the terraces. The differential GPS profiles clearly show that folding (and, presumably, movement

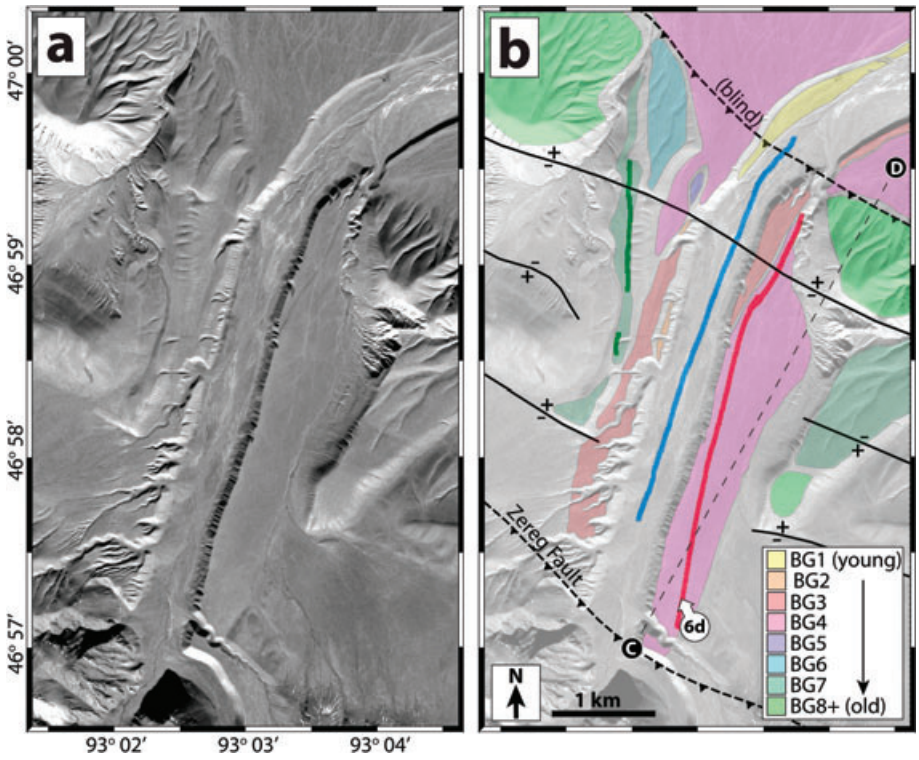

Figure 9. (a) SPOT 5 image of part of the forebergs in the southern Zereg Basin, where the Baatar Hyarhan Gol river exits the Baatar Hyarhan range. The location of the map is shown as a dashed box on Fig. 8. (b) The same view, with Late Quaternary terrace levels and fault scarps superimposed. The small green, red and blue squares are points measured in differential GPS profiles of the BG7, BG4 and abandoned Baatar Hyarhan Gol river bed surfaces, respectively; elevations are projected onto the line C–D and plotted in Fig. 10b.

on the underlying thrust) occurred during the Late Quaternary, but we are unable to quantify the rates of deformation.

4.3 Zereg fault

Our attention now shifts northwestwards along the Baatar Hyarhan range-front to the central section of the Zereg fault, adjacent to the highest part of the massif. Here, fresh NE-facing thrust scarps cut Quaternary alluvial fans deposited at the foot of the uplifting mountain range (Figs 8, 11 and 12). These fans are now abandoned, and streams flowing off Baatar Hyarhan actively incise into them. We found no fault exposures in river cuttings; however, because the scarps cross relatively steep fan deposits close to the range-front and have a fairly linear trace in map view, we infer that the fault dips quite steeply, perhaps ∼60°SW.

One of the clearest sections of faulting here is at 47°02′30″N 92°47′30″E (Figs 11a and 12b). At this locality, at least two levels of abandoned terrace are observed. The youngest and best preserved (called SZ1) is shaded red in Fig. 11(b); several small streams have incised into it, and recent debris-flows (consisting of scattered small boulders and gravels) coat the terrace surface close to these channels. There are also three isolated patches of an older terrace (or terraces), shaded in blue in Fig. 11(b). We used differential GPS to produce six topographic profiles perpendicular to the trace of the fault—four across SZ1 and two across the older surfaces (Fig. 13). The SZ1 surface is displaced vertically by 4.2–5.8 m across the fault scarp (up to the SW). The older surfaces are not preserved NE of the fault trace; so, we can only estimate minimum displacements; these are at least 8.7 m for the western patch and 29.5 m for the central one. The large difference between these values suggests that they are remnants of two separate surfaces.

Within this area, there are no natural cuttings into the terrace deposits in which sediment suitable for OSL dating might easily be collected. Instead, we dug a ∼1 m deep pit into the SZ1 surface; its precise position (at 47°02′27.5″N 92°47′35.4″E) was chosen to avoid any of the small stream channels or recent debris-flows, where there is a risk of dating material that postdates the terrace abandonment. The sediment exposed in the pit walls consists of 1–5 cm, angular gravels and a few larger clasts set in a fine-grained matrix. These high-energy deposits (possibly debris-flows) are not ideal for OSL sampling because of the reduced chance of exposure to sunlight during transport; however, with the scarps positioned so close to the range-front, lower-energy sediments may not be available at all. Using the second sampling method described in the Appendix (Section A1), we collected the finer matrix material from a depth of about 50 cm. This sample is labelled BH.

Luminescence measurements were taken using the laboratory methods outlined in Section A2. The large spread in equivalent dose values means that it is not clear which (if any) of the aliquots were reset before burial (Fig. A1b), and the burial age of $14.3 \pm {}_{1\sigma}$ 5.3 kyr—again calculated using the weighted mean equivalent dose—should be treated with caution (Table A2). However, the burial age is within error of that of a fan surface on the opposite margin of Baatar Hyarhan (see Section 4.4) and is similar to exposure ages calculated for a number of surfaces flanking the Gobi–Altai range in southern Mongolia (Vassallo *et al.* 2005; Ritz *et al.* 2006). Because of this, and given that we might expect alluvial sedimentation in the region to be pulsed (as it is in the Gobi–Altai), we are more confident that the burial age for SZ1 is correct. Combining the age with

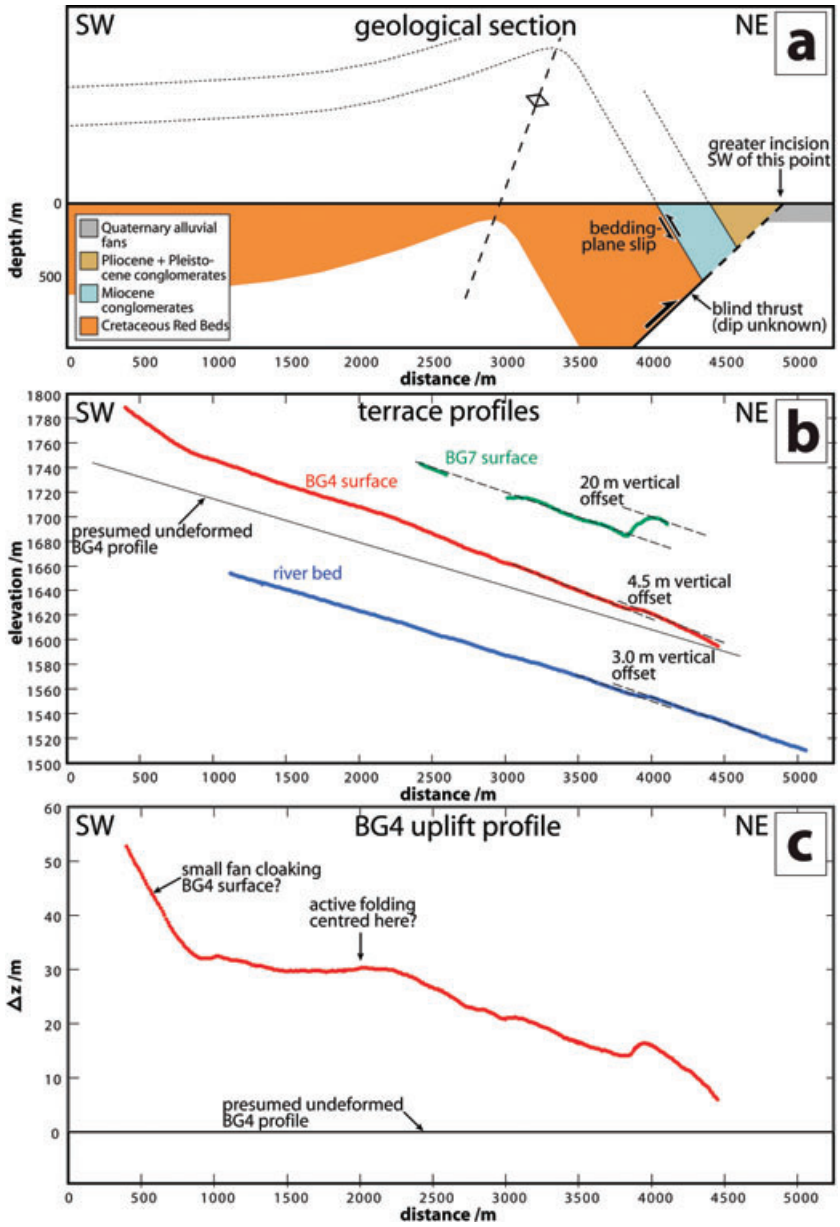

Figure 10. (a) Geological cross-section of the S Zereg Basin forebergs. Dip measurements are projected onto the line C–D (plotted on Fig. 9b). (b) Topographic profiles of the BG7 terrace (green), the BG4 terrace (red) and a prominent flood level of the Baatar Hyarhan Gol river bed (blue), all projected onto the line C–D (see Fig. 9b). (c) BG4 uplift profile, calculated by subtracting the presumed undeformed profile from the observed heights.

a vertical scarp offset of 5.0 ± 0.8 m gives a vertical displacement rate of $0.35^{+0.29}_{-0.14}$ mm yr^{-1} across the range-front fault. Using a range of dips from 50° to 70° SW yields a horizontal shortening rate of $0.20^{+0.34}_{-0.12}$ mm yr^{-1} and a slip rate of $0.40^{+0.44}_{-0.17}$ mm yr^{-1} (Table 1).

4.4 Tsetseg fault

Finally, we switch our attention to the southwestern margin of the range, where Baatar Hyarhan overthrusts the Tsetseg Basin along the Tsetseg fault. Here, fresh S- or SW-facing thrust scarps cut Quaternary alluvial fans, either right at the the foot of the range or a short distance (up to ∼1 km) out into the depression (Fig. 14). Northwest of ∼46°52′N 92°43′E, the active faulting passes through hilly terrain between the Tsetseg and Manhan basins.

Perhaps the clearest scarps along the Tsetseg fault are at 46°51′N 92°56′E (Figs 15a and 16a), where they cut abandoned and incised alluvial fans ∼500 m from the edge of the mountains. The same surfaces are not displaced across the range-front itself, which therefore appears to be inactive since fan abandonment. Again, there are no direct exposures of the fault in any river cuttings. However, striations and a ∼1-cm-thick layer of fault gouge are observed on the underside of a granitic vein that outcrops in a series of small bedrock exposures very close to the trace of the active faulting (Fig. 16b). Striated surfaces dip 32°–46° NNE, and the striations themselves indicate a small but significant component of right-lateral shear on the fault plane. In addition, schists, mylonites and volcanics (with a fabric dipping 40–70° N) exposed a few hundred metres north of the scarps are highly brecciated and foliated, indicating that the active faulting may follow the grain of an older shear zone.

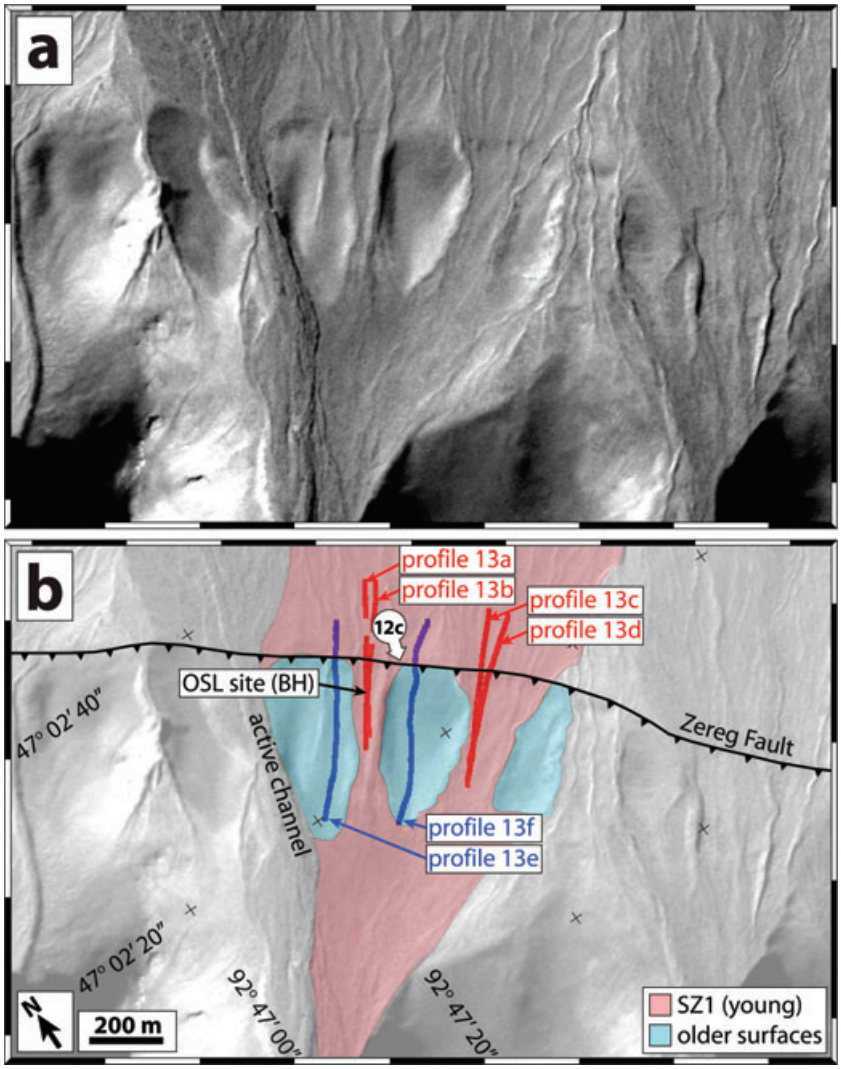

Figure 11. (a) SPOT 5 image of thrust scarps along the Zereg fault. The location of the map is shown as a dashed box on Fig. 8. (b) The same view, with terrace levels, fault scarps, exposed bedrock and differential GPS profile points superimposed.

Focusing on an alluvial fan (called NT1) rich in granite and, thus, easily distinguished by its light colour in SPOT imagery (Fig. 15b), we produced three topographic profiles across the fault with differential GPS (Fig. 17). The vertical displacement of NT1 across the scarp ranges from 2.5 to 3.3 m (up to the N). Following the procedures outlined in the Appendix (Section A1), we sampled the NT1 fan for OSL dating. Our sample, labelled TS, was taken from a sand lens exposed in a stream cutting at 46°50′50.9″N 92°45′45.5″E, ∼75 cm below the surface (Fig. 16c).

To measure the luminescence, we again employed the methods described in Section A2. Individual aliquot equivalent dose values form a broad peak (Fig. A1c), although the spread to this data suggests that bleaching was incomplete (as in Section 4.1). Using the weighted mean equivalent dose we attain a burial age of 20.0 $\pm_{1\sigma}$ 11.2 kyr (Table A2). Combining this age with a vertical scarp offset of 2.9 ± 0.4 m gives a vertical displacement rate of $0.15^{+0.23}_{-0.07}$ mm yr^{-1}. Using a fault dip of 39° ± 7°NNE, the horizontal shortening rate is $0.18^{+0.42}_{-0.10}$ mm yr^{-1} and the slip rate (neglecting the strike-slip component present in the striations) is $0.23^{+0.48}_{-0.12}$ mm yr^{-1} (Table 1).

5 DISCUSSION

5.1 OSL ages

One of the principle aims of this study was to investigate the applicability of OSL in dating alluvial sediments for slip-rate calculations. For all of our samples, the extent to which the luminescence signal was reset prior to burial is unknown; because of this, we use the weighted mean equivalent dose to calculate the OSL age, resulting in relatively large error bounds (particularly for the SZ1 surface). This uncertainty partly reflects the difficulty of finding suitable, fine-grained material so close to the active mountain-front. In addition, our measurements of the concentrations of radioactive K, U and Th within our samples—from which we estimate the dose-rate received during burial—may not be representative of the sediment as a whole. This adds a further uncertainty (one which is not reflected within our error bounds), and our ages should therefore be treated as preliminary only. However, OSL still provides very useful bounds on the age of these alluvial deposits, especially given the rarity of organic material for radiocarbon dating and the

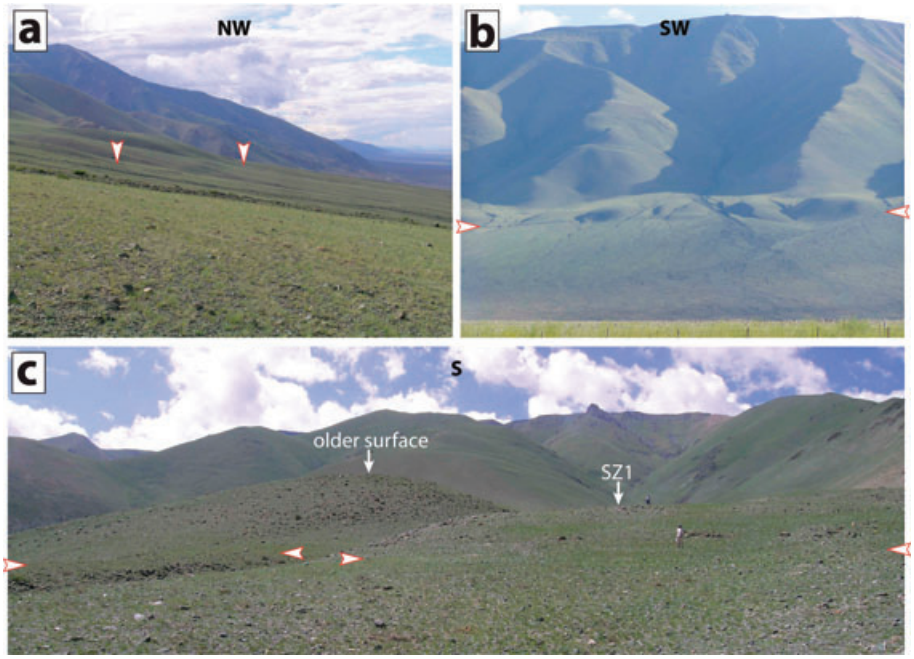

Figure 12. Photographs of the Zereg fault, with arrows picking out the base of thrust scarps. (a) View NW along the Baatar Hyarhan range-front from 47°01′50.3″N 92°48′51.9″E (see Fig. 8); NE-facing thrust scarps can be seen in the middle distance, just to the left-hand side of centre. (b) View SW from near the town of Zereg (see Fig. 8) of the fault scarps described in Section 4.3. (c) Close up of part of these same fault scarps, facing S from ∼47°02′30″N 92°47′40″E (see Fig. 11b). Two people at the top and bottom of the scarp provide scale.

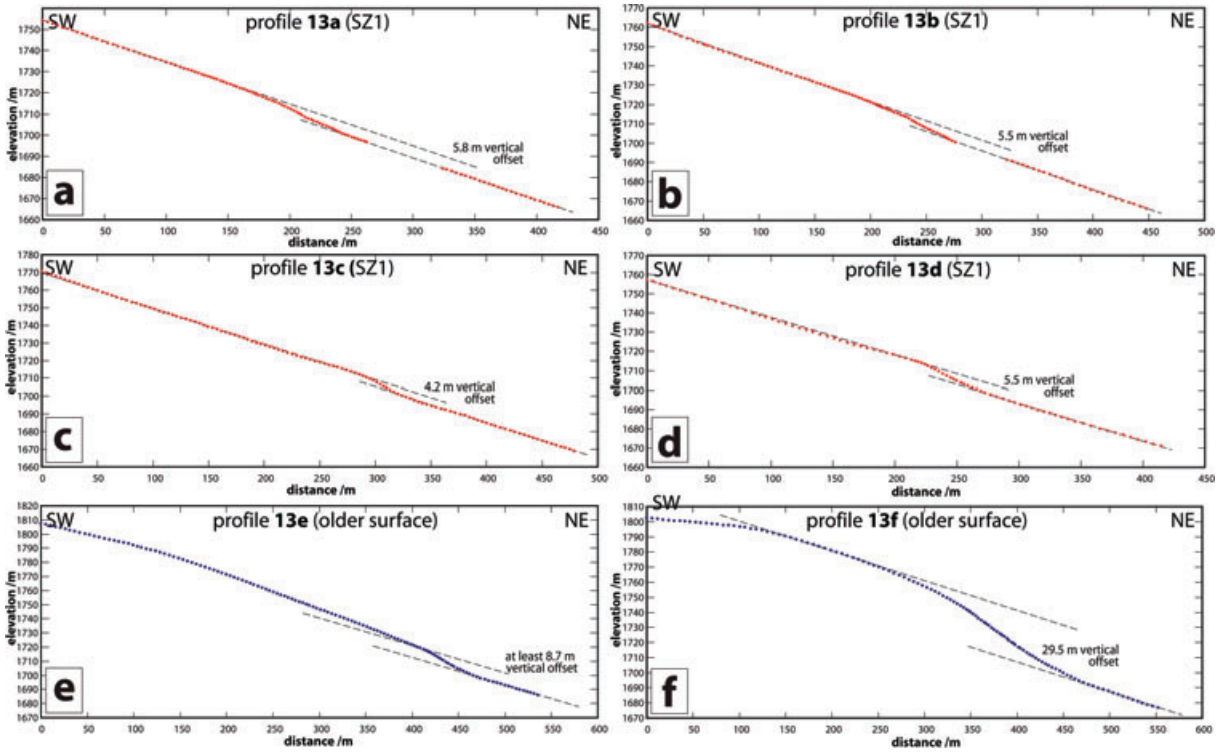

Figure 13. Topographic profiles of SZ1 fan (red) and older surfaces (blue), measured with differential GPS. Profile points are plotted on Fig. 11(b).

uncertainties in erosion rates, long-term cosmogenic isotope production rates and inherited isotope concentrations that complicate exposure dating.

The OSL ages of the SZ1 and NT1 alluvial fans (14.3 $\pm_{1\sigma}$ 5.3 kyr and 20.0 $\pm_{1\sigma}$ 11.2 kyr, respectively) agree well with figures of 15–20 kyr for fans in the Gobi Altai (a separate range in southern Mongolia), calculated with *in situ*-produced ^{10}Be (Vassallo *et al.* 2005; Ritz *et al.* 2006). In addition, the OSL age of the EZ2 terrace (84.1 $\pm_{1\sigma}$ 9.4 kyr) is close to a minimum age of 78 ± 11 kyr established for a strath terrace in the Gobi Altai, again using ^{10}Be

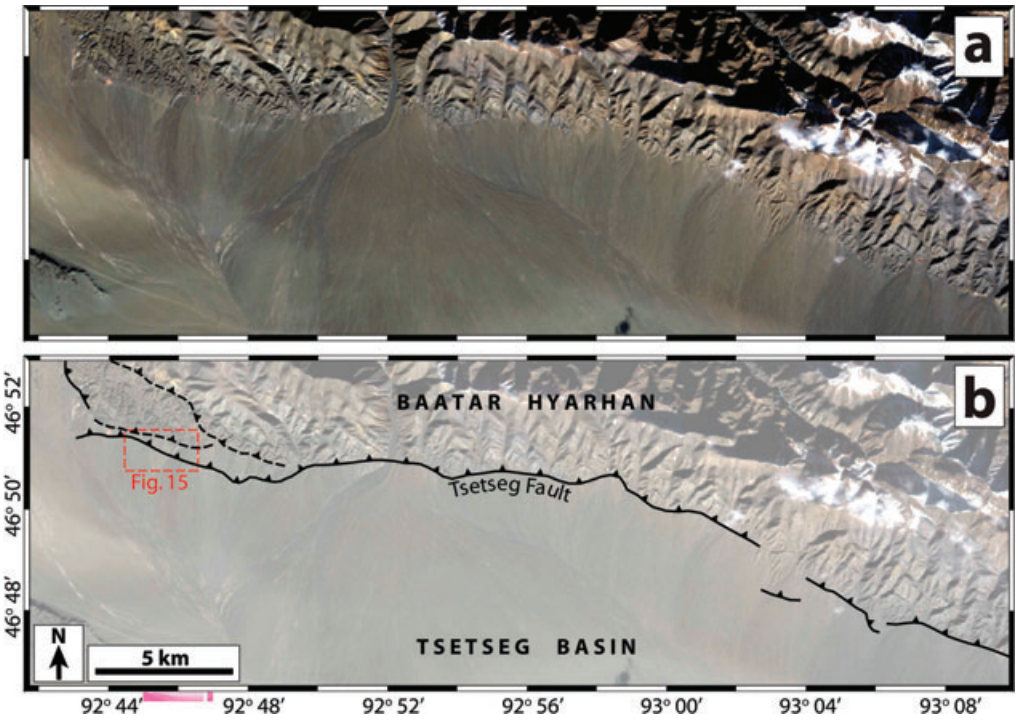

Figure 14. (a) ASTER image (RGB 321) showing the Tsetseg fault along the southwestern margin of Baatar Hyarhan. The location of the map is shown as a dashed box on Fig. 2. (b) The same view with active faults scarps plotted as thick solid lines; the dashed lines are older faults, probably now inactive.

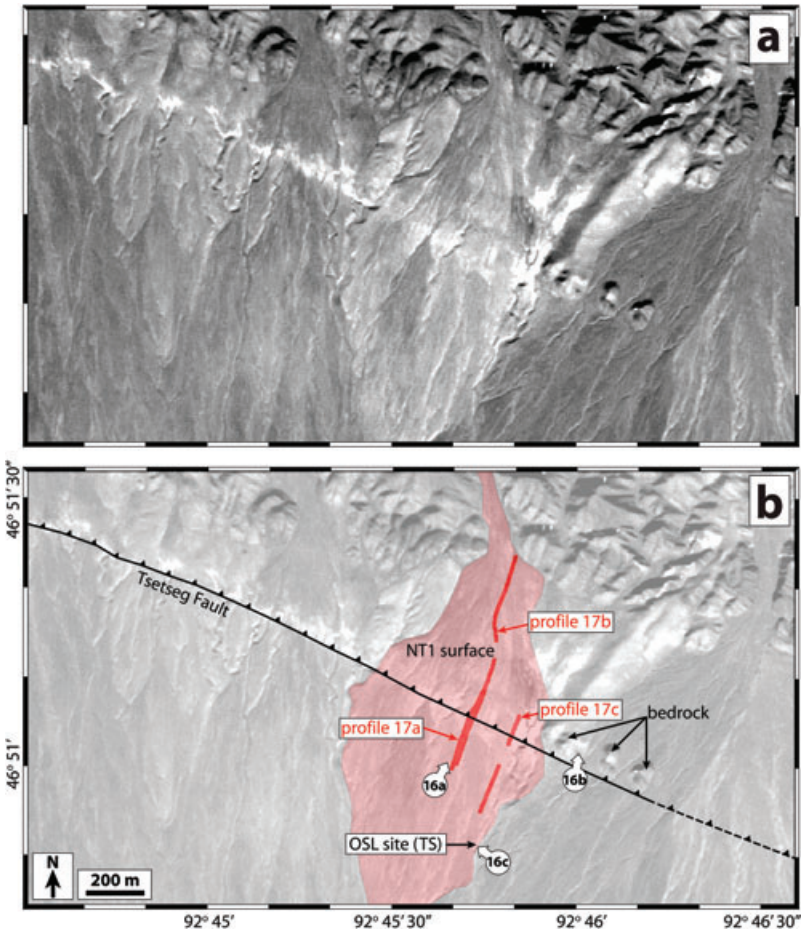

Figure 15. (a) SPOT 5 image of thrust scarps along the Tsetseg fault. The location of the map is shown as a dashed box on Fig. 14. (b) The same view, with the NT1 alluvial fan, fault scarps and differential GPS profile points superimposed.

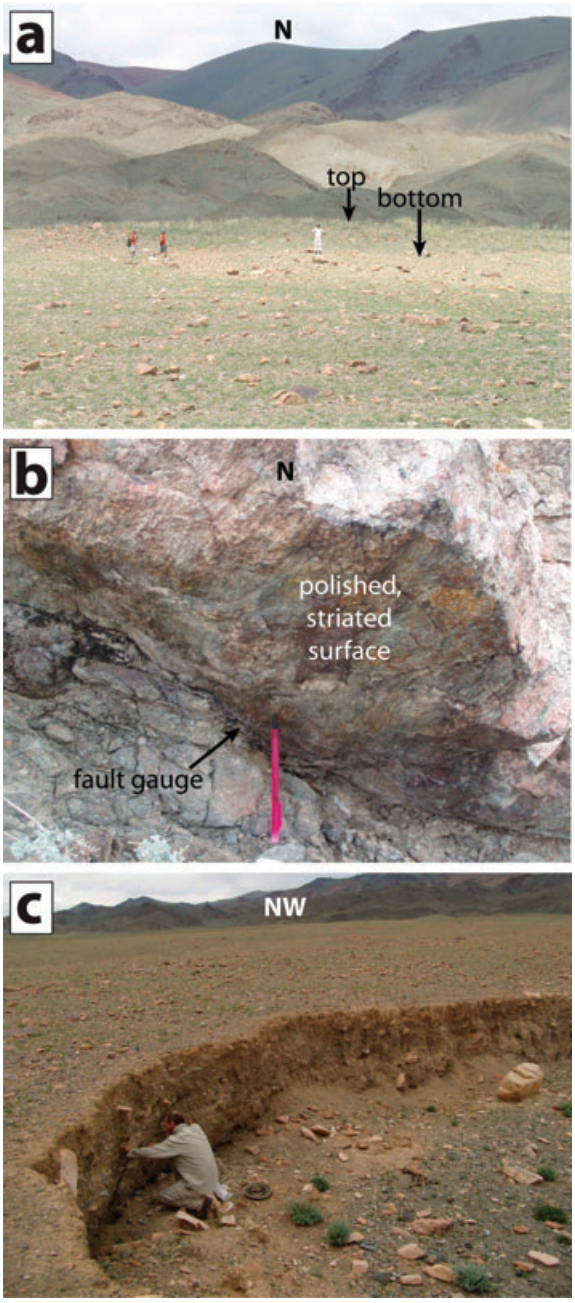

Figure 16. Photographs taken along the southwestern margin of Baatar Hyarhan (see Fig. 15 for locations). (a) View N from ∼46°51′00″N 92°45′40″E of the thrust scarp cutting the NT1 surface; three people standing at the foot of scarp provide scale. (b) Striations and a 1 cm thickness of fault gouge exposed on the underside of a NNE-dipping granite vein at 46°51′01.4″N 92°46′02.6″E; the view is to the N with a pencil for scale. (c) Sampling the NT1 fan for OSL dating at 46°50′50.9″N 92°45′45.5″E; the view is to the NW.

(Vassallo *et al.* 2007b). Our results hint that major periods of alluvial fan and river terrace formation in the Altai range in western Mongolia may correlate with those in the Gobi Altai, 400–500 km to the southeast. However, the ages of many more surfaces must be determined if this idea is to be tested fully, especially given the uncertainties in both dating methods.

5.2 Late Quaternary versus Geological deformation rates

We now compare our Late Quaternary vertical displacement rates across the Zereg and Tsetseg faults with long-term rates of range uplift, constrained by thermochronology and sedimentology (Section 3.2).

Before making this comparison, we must first consider the possibility that we are neglecting other active thrusts in the range interior. The clearest candidate for such a fault is a NE-dipping thrust, just south of the summit plateau (plotted on Fig. 2). However SPOT imagery reveals no fresh fault scarps along this thrust, and its contribution to the most recent uplift is likely to be negligible (we suspect that it results from an earlier stage of range uplift). Two more faults—one south of the summit plateau and one in the SE part of the range (Fig. 2)—show apparent right-lateral drainage displacements but are unlikely to contribute significantly to shortening and may not be active at all. We are therefore confident that our the slip-rate estimates do indeed bracket the total Late Quaternary vertical and horizontal displacement rates across the central part of the range.

According to the thermochronological work summarized in Section 3.2, the exhumation of bedrock exposed in Baatar Hyarhan (and presumably the uplift of the range above the surrounding depressions) started between 5 and 1 Ma (Vassallo 2006). Coarse alluvial sedimentation at the foot of the range, also discussed in this section, points to an earlier initiation of uplift, some time in the Miocene (Howard *et al.* 2003). An age of 5 Myr minimizes the discrepancy between these two estimates, and we use this value in our subsequent calculations.

To determine the long-term vertical displacement rates across the range-bounding faults, we use the Late Mesozoic erosional surface as a marker. On Baatar Hyarhan itself, the summit peneplain is at 3600 m elevation; erosion rates are probably low (Jolivet *et al.* 2007) and for the purposes of our calculation, can be ignored. In the central Zereg Basin (elevation ∼1100 m), the peneplain is covered by an estimated sediment thickness of ∼1500 m (see Fig. 7a), giving a total ∼4000 m vertical displacement. However, the marker may be deeper here than at the range-front, due to crustal flexure caused by the uplift of Baatar Hyarhan and Bumbat Nuruu and subsidence caused by the weight of Late Cenozoic sediments shed into the basin; we therefore consider 4000 m a maximum estimate of the displacement across the Zereg fault itself. A minimum estimate of 1900 m is calculated by subtracting the elevation of the Zereg fault scarps (1700 m) from that of the summit peneplain (3600 m). The total offset across the Zereg fault is thus bracketed at 1900–4000 m. Using the same arguments (and assuming an equivalent sediment thickness) in the Tsetseg Basin, we bracket the total offset across the Tsetseg fault at 1400–3400 m.

Dividing these values by the age of 5 Myr gives long-term vertical displacement rates of ∼0.4–0.8 and ∼0.3–0.7 mm yr^{-1} across the NE and SW margins of the range, respectively. In comparison, ∼20 kyr displacement rates are 0.2–0.6 mm yr^{-1} across the Zereg fault and 0.1–0.4 mm yr^{-1} across the Tsetseg fault. Our Late Quaternary vertical displacement rates are therefore at the lower bounds of the geological rates.

Vertical rates of deformation may, therefore, have remained constant over the past ∼5 Ma (at 0.4–0.6 mm yr^{-1} across the Zereg fault and 0.3–0.4 mm yr^{-1} across the Tsetseg fault), but equally the Late Quaternary rates might be lower than the geological ones. This possible discrepancy could be explained by the migration of some shortening away from the range-bounding faults and onto new structures in neighbouring low-lying areas, presumably in response

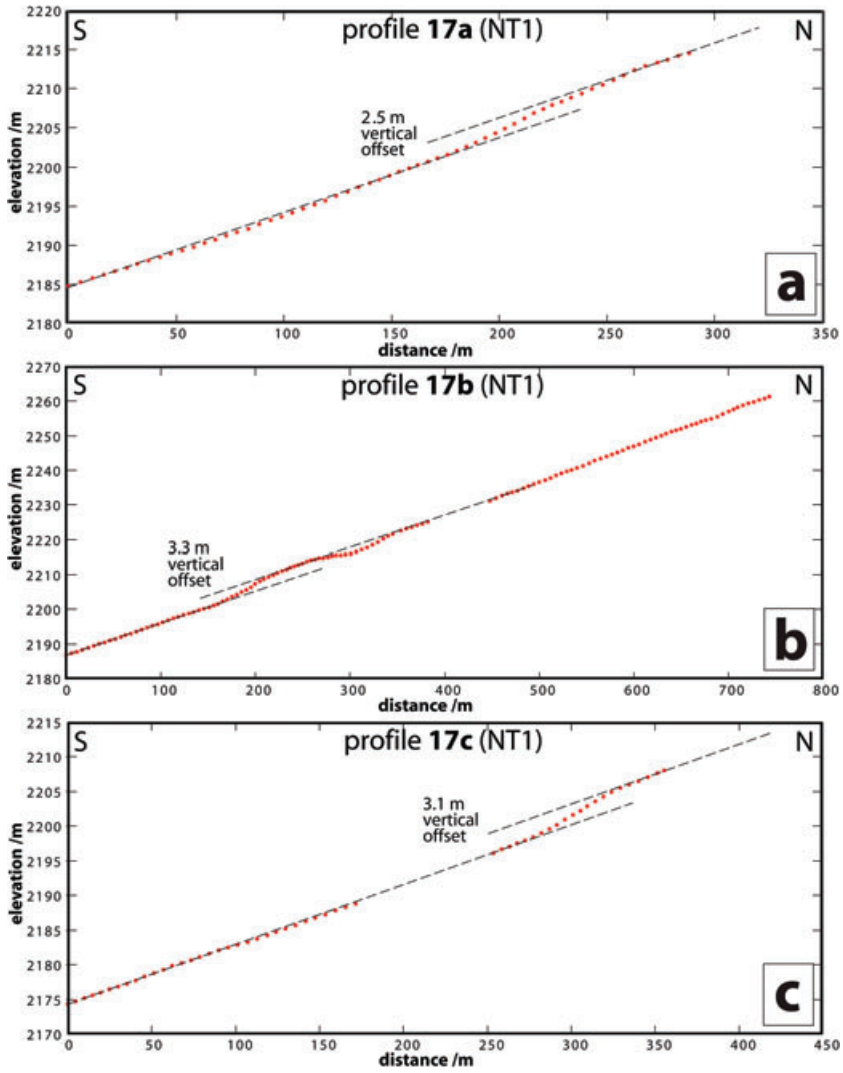

Figure 17. Topographic profiles of NT1 fan surface, measured with differential GPS. Profile points are plotted on Fig. 15(b).

to stresses generated by the raised topography. There are numerous other ∼4–4.5 km peaks across the Altai, but none that are higher; perhaps once these elevations are achieved, the migration of fault activity away from the high areas is triggered. Certainly, there are many examples of similar behaviour in other parts of deforming Asia (e.g. Avouac *et al.* 1993; Bayasgalan *et al.* 1999b).

Geomorphic evidence from the SE section of Baatar Hyarhan supports the idea that active faulting has shifted away from the range-front into the southern Zereg Basin forebergs. However, the apparent slowing of vertical displacement rates alongside central Baatar Hyarhan cannot be explained by a switch in fault activity to the eastern Zereg Basin; our structural model implies at least 10 km overall shortening here, which (at our estimated Late Quaternary rates) would be achieved in 8–17 Myr. This age could be reduced (and Late Quaternary shortening rates increased) if some of the convergence across the forebergs is accommodated by folding not accounted for in our estimate, or if shortening was faster prior to ∼85 ka (the age of the EZ2 terrace). But the onset of deformation in the eastern Zereg Basin is still unlikely to be much younger than in the Baatar Hyarhan range itself; indeed, from the available data, it is possible that the eastern Zereg Basin forebergs are similar in age, or even older, than Baatar Hyarhan. The forebergs cannot, therefore, be regarded simply as the latest phase of outward mountain growth.

There are other ways in which the possible discrepancy between ∼20 kyr and ∼5 Myr year rates of range uplift could be accounted for. Feasible explanations include a shift in deformation to outside the area studied here or a reduction in the overall rate of shortening across the Altai. Another possibility is that the sediment thickness in the Zereg Basin is lower than the figure suggested by our structural model, reducing the total throw on the range-front faults and, in turn, the long-term rates of range uplift. Equally, if our preliminary OSL ages are too old (due to the problem of incomplete bleaching) then the Late Quaternary rates should be higher. Clearly the uncertainties in our structural model and (in particular) our OSL ages make it difficult to discriminate between these different interpretations.

5.3 Late Quaternary versus decadal deformation rates

The relatively sparse GPS coverage in the Altai (Fig. 1) provides no direct measurement of shortening across Baatar Hyarhan on decadal timescales. Nevertheless, it is useful to compare our Late

Quaternary horizontal displacement rates with GPS estimates of shortening across the whole Altai, to assess the contribution Baatar Hyarhan makes to this total convergence.

All three areas for which we have Late Quaternary slip-rate estimates are adjacent to, or opposite, the central and highest part of Baatar Hyarhan. Adding up the horizontal displacement rates across these areas gives a total shortening rate of 0.7–2.4 mm yr^{-1}. The current rate of convergence across the whole Altai range, measured with GPS, is ∼7 mm yr^{-1} (Calais *et al.* 2003). Late Quaternary shortening across Baatar Hyarhan and the Zereg Basin thus makes up between one tenth and one third of this total. The majority of convergence is likely to be accommodated by the anticlockwise rotation of the dextral strike-slip faults and the slivers of crust between them.

6 CONCLUSIONS

We investigate a series of clear thrust scarps in Late Quaternary alluvial deposits at the margins of Baatar Hyarhan, a major massif in the Mongolian Altai mountains. OSL provides useful bounds on the age of these deposits, despite significant uncertainties in the extent to which each sample was bleached prior to burial. We calculate ∼20 kyr vertical displacement rates of 0.2–0.6 and 0.1–0.4 mm yr^{-1} across the NE and SW margins of Baatar Hyarhan, respectively. Our results are at the lower end of long-term (5 Myr) estimates of vertical displacement rates across the same margins, which are ∼0.4–0.8 and 0.3–0.7 mm yr^{-1}, respectively . The possible disparity between Late Quaternary and geological rates could be explained if some shortening has migrated away from the range-bounding thrusts in response to stresses introduced by topography, although the large uncertainties in slip rates prevent us from ruling out other possibilities. Today, the forebergs in the eastern Zereg Basin accommodate a large part of the shortening across the study area. However, these are unlikely to be younger than Baatar Hyarhan itself and cannot be seen as simply the latest stage of outward mountain growth. Overall, thrust faulting around the Baatar Hyarhan massif and in the eastern Zereg Basin accommodates around 0.7–2.4 mm yr^{-1} of the overall ∼7 mm yr^{-1} convergence across the Altai mountains.

ACKNOWLEDGMENTS

This work was supported by NERC funding of COMET (http://comet.nerc.ac.uk) and a NERC studentship to Edwin Nissen, and SPOT imagery was made available through the OASIS programme (http://medias.obs-mip.fr/oasis). Contributions in the field from Dr Tien and Dr Zhang from the Chinese Earthquake Administration are gratefully acknowledged. We also thank our driver, Baatar, and student helpers, Baatar, Buyanaa, Deegii, Esukhei and Jakii, for their hard work and good company in the field, Ganbold for his kind hospitality in Hovd and Chimgee and Altan for their help in Ulaan Baatar. Finally, the paper benefited from comments on an early draft by John Elliott and detailed reviews by Tim Byrne and Riccardo Vassallo.

REFERENCES

Aitken, M.J., 1985. *Thermoluminescence Dating*, Academic Press, London.

Avouac, J.-P., Tapponnier, P., Bai, M., You, H. & Wang, G., 1993. Active thrusting and folding along the northern Tien Shan and Late Cenozoic rotation of the Tarim relative to Dzungaria and Kazakhstan, *J. geophys. Res.*, **98,** 6755–6804.

Baljinnyam, I. *et al.*, 1993. *Ruptures of Major Earthquakes and Active Deformation in Mongolia and Its Surroundings*, Memoir 181, Geol. Soc. Am., 62 pp.

Bayasgalan, A., Jackson, J., Ritz, J.-F. & Carretier, S., 1999a. Field examples of strike-slip fault terminations in Mongolia and their tectonic significance, *Tectonics*, **18**(3), 394–411.

Bayasgalan, A., Jackson, J., Ritz, J.-F. & Carretier, S., 1999b. 'Forebergs', flower structures, and the development of large intra-continental strike-slip faults: the Gurvan Bogd fault system in Mongolia, *J. Struct. Geol.*, **21,** 1285–1302.

Bayasgalan, A., Jackson, J. & McKenzie, D., 2005. Lithosphere rheology and active tectonics in Mongolia: relations between earthquake source parameters, gravity and GPS measurements, *Geophys. J. Int.*, **163,** 1151–1179.

Bell, W.T., 1980. Alpha dose attenuation in quartz grains for thermoluminescence dating, *Ancient TL*, **12,** 4–8.

Calais, E., Vergnolle, M., San'kov, V., Lukhnev, A., Miroshnitchenko, A., Amarjargal, S. & Déverchère, J., 2003. GPS measurements of crustal deformation in the Baikal–Mongolia area (1994–2002): implications for current kinematics of Asia, *J. geophys. Res.*, **108**(B10), 2501, doi:10.1029/2002JB002373.

Chen, Z. *et al.*, 2000. Global positioning system measurements from eastern Tibet and their implications for India/Eurasia intercontinental deformation, *J. geophys. Res.*, **105,** 16 215–16 228.

Cunningham, W.D., 1998. Lithospheric controls on late Cenozoic construction of the Mongolian Altai, *Tectonics*, **17,** 891–902.

Cunningham, D., 2005. Active intracontinental transpressional mountain building in the Mongolian Altai: defining a new class of orogen, *Earth planet. Sci. Lett.*, **240,** 436–444.

De Grave, J. & Van den haute, P., 2002. Denudation and cooling of the Late Teleskoye Region in the Altai Mountains (South Siberia) as revealed by apatite fission-track thermochronology, *Tectonophysics*, **349,** 145–159.

Devyatkin, E.V., 1974. Structures and formational complexes of the Cenozoic activated stage (in Russian), in *Tectonics of the Mongolian People's Republic*, pp. 182–195, Nauka, Moscow.

Devyatkin, E.V., 1981. *The Cenozoic of Inner Asia* (in Russian), Nauka, Moscow.

Engdahl, E.R., van der Hilst, R.D. & Buland, R., 1998. Global teleseismic earthquake relocation from improved travel times and procedures for depth determination, *Bull. seism. Soc. Am.*, **88,** 722–743.

Florensov, N.A. & Solonenko, V.P., 1963. *The Gobi-Altay earthquake (in Russian)*, Academika Nauk USSR, Moscow (English translation, U.S. Department of Commerce, Washington, D.C., 1965).

Howard, J.P., Cunningham, W.D., Davies, S.J., Dijkstra, A.H. & Badarch, G., 2003. The stratigraphic and structural evolution of the dzereg basin, western mongolia: clastic sedimentation, transpressional faulting and basin destruction in an intraplate, intracontinental setting, *Basin. Res.*, **15**(1), 45–72.

Jolivet, M. *et al.*, 2007. Mongolian summits: an uplifted, flat, old but still preserved erosion surface, *Geology*, **35**(10), 871—874.

Keller, E.A., Zepeda, R.L., Rockwell, T.K., Ku, T.L. & Dinklage, W.S., 1998. Active tectonics at Wheeler Ridge, Southern San Joaquin Valley, California, *Geol. Soc. Am. Bull.*, **110,** 298–310.

Keller, E.A., Gurrola, L. & Tierney, T.E., 1999. Geomorphic criteria to determine direction of lateral propagation of reverse faulting and folding, *Geology*, **27,** 515–518.

Mejdahl, V., 1979. Thermoluminescence dating: beta-dose attenuation in quartz grains, *Archaeometry*, **21,** 61–72.

Murray, A.S. & Wintle, A.G., 2000. Luminescence dating of quartz using an improved single-aliquot regenerative-dose protocol, *Rad. Measure.*, **32,** 57–73.

Nissen, E., Emmerson, B., Funning, G.J., Mistrukov, A., Parsons, B., Robinson, D.P., Rogozhin, E. & Wright, T.J., 2007. Combining InSAR and seismology to study the 2003 Siberian Altai earthquakes-dextral strike-slip and anticlockwise rotations in the northern India-Eurasia collision zone, *Geophys. J. Int.*, **169,** 216–232.

Owen, L.A., Windley, B.F., Cunningham, W.D., Badamgarav, J. & Dorjnamjaa, D., 1997. Quaternary alluvial fans in the Gobi of southern Mongolia:

evidence for neotectonics and climate change, *J. Quat. Sci.,* **12**(3), 239–252.

Owen, L.A., Cunningham, D., Richards, B.W.M., Rhodes, E., Windley, B.F., Dorjnamjaa, D. & Badamgarav, J., 1999. Timing of formation of forebergs in the northeastern Gobi Altai, Mongolia: implications for estimating mountain uplift rates and earthquake recurrence intervals, *J. geol. Soc. Lond.,* **156**(3), 457–464.

Pan, B., Burbank, D., Wang, Y., Wu, G., Li, J. & Guan, Q., 2003. A 900 k.y. record of strath terrace formation during glacial-interglacial transitions in northwest China, *Geology,* **31,** 957–960.

Prescott, J.R. & Hutton, J.T., 1988. Cosmic ray and gamma ray dosimetry for TL and ESR, *Nucl. Tracks Rad. Meas.,* **14,** 223–227.

Ritz, J.-F., Vassallo, R., Braucher, R., Brown, E.T., Carretier, S. & Bourlès, D.L., 2006. Using in situ-produced ^{10}Be to quantify active tectonics in the Gurvan Bogd mountain range (Gobi-Altay, Mongolia), in *In Situ-Produced Cosmogenic Nuclides and Quantification of Geological Processes,* Special Papers No. 415, pp. 87–110, Geological Society of America.

Schermer, E.R., Luyendyk, B.P. & Cisowski, S., 1996. Late Cenozoic structure and tectonics of the northern Mojave Desert, *Tectonics,* **15,** 905–932.

Sella, G.F., Dixon, T.H. & Mao, A., 2002. REVEL: a model for Recent plate velocities from space geodesy, *J. geophys. Res.,* **107**(B4), 2081, doi:10.1029/2000JB000033.

Sengör, A.M.C., Natal'in, B.A. & Burtman, V.S., 1993. Evolution of the Altaid tectonic collage and Palaeozoic crustal growth in Eurasia, *Nature,* **364,** 299–307.

Suppe, J., 1983. Geometry and kinematics of fault-bend folding, *Amer. J. Sci.,* **283,** 684–721.

Suppe, J. & Medwedeff, D.A., 1990. Geometry and kinematics of fault-propogation folding, *Eclogae Geol. Helvetiae,* **83,** 409–454.

Tapponnier, P. & Molnar, P., 1979. Active faulting and Cenozoic tectonics of the Tien Shan, Mongolia, and Baykal regions, *J. geophys. Res.,* **84,** 3425–3459.

Thomas, J.C., Lanza, R., Kazansky, A., Zykin, V., Semakov, N., Mitrokhin, D. & Delvaux, D., 2002. Paleomagnetic study of Cenozoic sediments from the Zaisan basin (SE Kazakhstan) and the Chuya depression (Siberian Altai): tectonic implications for central Asia, *Tectonophysics,* **351,** 119–137.

Vassallo, R., 2006. Chronologie et évolution des reliefs dans la région de Mongolie-Sibérie: approche morphotectonique et géochronologique (in French), *PhD thesis,* Université Montpellier 2, Montpellier.

Vassallo, R., Ritz, J.F., Braucher, R. & Carretier, S., 2005. Dating faulted alluvial fans with cosmogenic^{10}Be in the Gurvan Bogd mountain range (Gobi-Altay, Mongolia): climatic and tectonic implications, *Terra Nova,* **17,** 278–285.

Vassallo, R., Jolivet, M., Ritz, J.-F., Braucher, R., Larroque, C., Sue, C., Todbileg, M. & Javkhlanbold, D., 2007a. Uplift age and rates of the Gurvan Bogd system (Gobi-Altay) by apatite fission track analysis, *Earth planet. Sci. Lett.,* **259,** 333–346.

Vassallo, R. *et al.,* 2007b. Transpressional tectonics and stream terraces of the Gobi-Altay, Mongolia, *Tectonics,* **26,** C5013+.

Walker, R. & Jackson, J., 2004. Active tectonics and late Cenozoic strain distribution in central and eastern Iran, *Tectonics,* **23,** TC5010, doi:10.1029/2003TC001529.

Walker, R.T. *et al.,* 2006. Geomorphology and structure of the Jid right-lateral strike-slip fault in the Mongolian Altay mountains, *J. Struct. Geol.,* **28,** 1607–1622.

Wang, Q. et al., 2001. Present-day crustal deformation in China constrained by global positioning system measurements, *Science,* **294,** 574–578.

Yielding, G., Jackson, J.A., King, G.C.P., Sinvhal, H., Vita-Finzi, C. & Wood, R.M., 1981. Relations between surface deformation, fault geometry, seismicity, and rupture characteristics during the El Asnam (Algeria) earthquake of 10 October 1980, *Earth planet. Sci. Lett.,* **56,** 287–304.

Yuan, W., Carter, A., Dong, J. & Bao, Z., 2006. Mesozoic-Tertiary exhumation history of the Altai Mountains, northern Xinjiang, China: new constraints from apatite fission track data, *Tectonophysics,* **412,** 183–193.

Zaitsev, N.S., Kovalenko, V.I., Luvsandansan, B., Lutchiski, I.V. & Yarmolyuk, V.V., 1989. Geological map of the People's Republic of Mongolia, 1/500,000, Academy of Sciences, People's Republic of Mongolia.

APPENDIX A: OPTICALLY STIMULATED LUMINESCENCE (OSL) DATING

We use OSL dating to estimate the deposition age of the alluvial sediments used as markers of cumulative fault movement. Ionizing radiation—from the decay of ^{238}U, ^{232}Th and ^{40}K in the surrounding sediment and from cosmic rays—displaces lattice-bound electrons within quartz and feldspar grains. These electrons can become stored in lattice defects in these minerals, although they are released upon exposure to light. Once the grains are buried, the trapped electrons can begin to accumulate, and the luminescence clock begins. Fine-grained fluvial or aeolian sediments are preferred for OSL dating, because they are likely to have undergone prolonged exposure to sunlight during transport, thus resetting the luminescence clock prior to deposition. Stimulating samples of buried quartz and feldspar grains with visible light in the laboratory releases the trapped electrons, along with photons of light (luminescence). The age at which this sediment was last exposed to light is determined by dividing the amount of radiation required to reproduce the observed luminscence (known as the equivalent dose, D_e) by the dose rate received during burial (calculated using measurements of U, Th and K within the surrounding sediment and from estimates of cosmic radiation).

A1 Sampling

Our sampling was done at dusk, in order to reduce the risk of accidental exposure to full sunlight. For two of the samples (ZE and TS) we cut a fresh surface into the exposed sand layer, into which a metal tube was inserted (we used empty, steel food cans). The tube was removed and the open end covered with duct-tape to ensure as little light as possible reached the uppermost sediment inside. We then packed the tube tightly with more duct-tape to prevent the material inside from shifting during transport, and wrapped the tube in several layers of opaque black plastic.

Table A1. Generalized single aliquot regeneration (SAR) sequence for OSL samples, after Murray & Wintle (2000). We give four regeneration doses (L_x, $x = 1, 2, 3, 4$). Sensitivity changes of the regenerated OSL data are corrected by dividing L_x by the subsequent OSL test dose response (T_x, $T = 1, 2, 3, 4$). We plot the corrected OSL (L_x/T_x) against the regenerative dose and apply a linear fit to the data points. The equivalent dose (D_e) corresponding to the natural OSL response (L_N/T_N) is then read from the regenerative dose axis.

Step	Treatment	Observed
1	Give dose	–
2	Preheat (260°C for 10 s)	–
3	Stimulation (for 100 s at 125°C)	L_x
4	Give test dose	–
5	Preheat (220°C for 10 s)	–
6	Stimulation (for 100 s at 125°C)	T_x
7	Return to Step 1	–

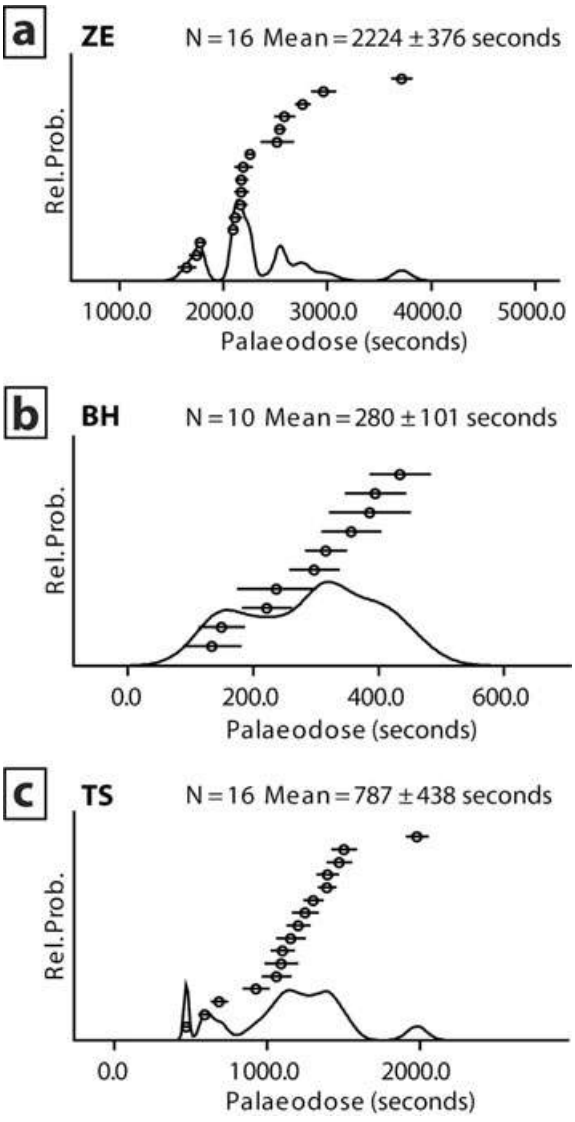

Figure A1. Equivalent dose distribution plots for OSL samples. The *x*-axis represents the number of seconds of exposure to a known beta source (delivering ∼5 Gyr min^{-1}) required to reproduce the natural luminescence signal. There are N aliquots in each sample, and Mean is the weighted mean D_e for all these aliquots. Individual aliquot D_e values are displayed in rank order, with probability density functions superimposed. For (a) ZE and (c) TS, D_e values form a well-defined peak; however, there is still a significant spread to the data, suggesting that bleaching of these samples was incomplete. For (b) BH, there is no clear peak to the dose distribution plot; so, we cannot be certain that any of the aliquots were reset during transport prior to burial.

For the final sample (BH), the sediment exposed in the pit walls was too coarse to insert a tube and not cohesive enough to extract a large block. Instead, the pit was covered with canvas and plastic to ensure that sampling was done in darkness. Inside the pit, we widened one of the pit walls to remove any sediment that might have been exposed during digging. Using a sieve to remove larger clasts, we scraped loose, fine-grained matrix material from the widened pit wall into light-protected bags.

A2 Laboratory work

In the laboratory, under subdued red light, we removed sediment from the top and bottom of each tube (this may have undergone some exposure to light during sampling). Later on, we used this top and bottom material to estimate the dose rates received during burial. We are confident that no light entered the central part of the tube, and it is only this material that we used to determine D_e. The samples were wet-sieved, and the 90–250 μm fraction immersed for 2 d in 1 N HCl and 2 d in H_2O_2 to eliminate carbonates and organics, respectively. Heavy minerals (>2.72 g cm^{-3}) were then removed in a heavy liquid separation. The remaining quartz grains were etched in 48 per cent HF for 6 min, rinsed in distilled water and dry-sieved. The 90–250 μm fraction was mounted as a monolayer on 10 mm diameter aluminium discs, using a silicon spray as an adhesive. Between 10 and 16 such discs are prepared from each sample. These were stimulated using a Risø (Model TL/OSL-DA-15) automated TL/OSL system with a ^{90}Sr/^{90} Y beta source delivering ∼5 Gyr min^{-1}. An IR laser diode ($\lambda = 830$ nm) and blue diode array ($\lambda = 470$ nm, $p = 24$ mW cm^{-2}) provided the samples with laser light of ∼400 mW cm^{-2} intensity. OSL was detected with an Electron Tubes bialkaline PMT and the luminescence measured through 7 mm Hoya U-340 filters. To determine D_e, we followed the single aliquot regeneration (SAR) protocol of Murray & Wintle (2000) and the steps detailed in Table A1.

Individual aliquot D_e values are plotted with a probability density function in Fig. A1. For all three samples, there is a significant spread to this data; so, we cannot be certain that they were completely bleached prior to burial. We therefore use the weighted mean D_e (given in Table A2) to determine the burial age.

Dose-rates received by each sample during burial were calculated using radioisotope concentrations, present-day moisture content and burial depths. Concentrations of U, Th and K were measured in the laboratory with ICP mass spectroscopy, and moisture contents determined by drying at 40 °C. We use the conversion factors of Aitken (1985), Bell (1980) and Mejdahl (1979) to calculate the resulting alpha, beta and gamma dose rates. Dose rates received from cosmic rays are determined using the formula of Prescott & Hutton (1988).

Table A2. Values used to calculate luminescence ages for the three fan surfaces. The errors are all 1σ. Sample ZE is taken from the eastern Zereg Basin forebergs (EZ2 surface), BH from the NE Baatar Hyarhan range-front (SZ1 surface) and TS from the SW Baatar Hyarhan range-front (NT1 surface).

Sample	Equivalent dose (Gyr)	K (per cent)	U (ppm)	Th (ppm)	Cosmic dose rate (Gyr kyr^{-1})	Total dose rate (Gyr kyr^{-1})	Age (ktr)
ZE	188.29 ± 15.89	1.519 ± 0.028	1.4 ± 0.052	3.6 ± 0.168	0.181 ± 0.135	2.24 ± 0.15	84.1 ± 9.4
BH	22.93 ± 8.27	1.046 ± 0.028	0.7 ± 0.052	2.0 ± 0.168	0.284 ± 0.135	1.60 ± 0.14	14.3 ± 5.3
TS	64.46 ± 35.87	1.909 ± 0.028	2.1 ± 0.052	8.4 ± 0.168	0.288 ± 0.135	3.23 ± 0.16	20.0 ± 11.2